Electron-spin spectral diffusion in an erbium doped crystal at millikelvin temperatures

M. Rančić[1a)], M. Le Dantec[1a)], S. Lin[2], S. Bertaina[3], T. Chanelière[4], D. Serrano[5], P. Goldner[5], R. B. Liu[2], E. Flurin[1], D. Estève[1], D. Vion[1], P. Bertet[1*]

[1] *Université Paris-Saclay, CEA, CNRS, SPEC, 91191 Gif-sur-Yvette Cedex, France*

[2] *Department of Physics, Centre for Quantum Coherence, and The Hong Kong Institute of Quantum Information Science and Technology, The Chinese University of Hong Kong, Shatin, New Territories, Hong Kong, China*

[3] *CNRS, Aix-Marseille Université, IM2NP (UMR 7334), Institut Matériaux Microélectronique et Nanosciences de Provence, Marseille, France*

[4] *Univ. Grenoble Alpes, CNRS, Grenoble INP, Institut Néel, 38000 Grenoble, France*

[5] *Chimie ParisTech, PSL University, CNRS, Institut de Recherche de Chimie Paris, 75005 Paris, France*

[6] *Walther Meissner Institut, Bayerische Akademie der Wissenschaften, Garching, Germany*

Erbium-doped crystals offer a versatile platform for hybrid quantum devices because they combine magnetically-sensitive electron-spin transitions with telecom-wavelength optical transitions. At the high doping concentrations necessary for many quantum applications, however, strong magnetic interactions of the electron-spin bath lead to excess spectral diffusion and rapid decoherence. Here we lithographically fabricate a 4.4 GHz superconducting planar micro-resonator on a $CaWO_4$ crystal doped with Er ions at a concentration of twenty parts per million relative to Ca. Using the microwave resonator, we characterize the spectral diffusion processes that limit the electron-spin coherence of Er ions at millikelvin temperatures by applying 2- and 3-pulse echo sequences. The coherence time shows a strong temperature dependence, reaching 1.3 ms at 23 mK for an electron-spin transition of ^{167}Er.

I. INTRODUCTION

Rare earth ion doped materials cooled to liquid helium temperatures have demonstrated long coherence times [1–4] and large efficiencies for quantum memory demonstrations in the optical domain [5–7]. Recently, interest in these materials has extended to sub-Kelvin temperatures and sub-Tesla fields, where the electron-spin transitions of Kramers (odd-electron) rare-earth ions achieve gigahertz frequencies while exceeding the energy of the thermal bath. This interest is motivated by the prospect of ensemble-based microwave-to-optical conversion [8, 9] and microwave quantum memories [10, 11], both of which require long electron-spin coherence times and sufficient concentration for high-fidelity operation. Previous demonstrations of ensemble-based microwave quantum memories required concentrations of electron-spins between one and one hundred parts per million (ppm) to achieve storage efficiencies of order 10^{-3} [12–14].

Several rare-earth doped materials have also demonstrated millisecond-scale electron-spin coherence [15, 16] and hybridised electron-nuclear-spin coherence [17, 18] with these applications in mind. Amongst these proposed materials, erbium doped calcium tungstate (Er^{3+}:$CaWO_4$) has emerged as a leading candidate due to its telecom-wavelength optical transition and ∼20 ms coherence both predicted [19, 20] and measured [19] on a magnetically-sensitive electron-spin transition. This demonstration of long coherence was attributed to a millikelvin spin-bath temperature combined with an ultra-low Er doping concentration of just 0.7 ppb, yielding a regime in which the weak magnetic interaction with the ^{183}W nuclear-spin bath dictated the electron-spin decoherence rate.

At higher doping concentrations that are required for quantum applications, however, the strong magnetic interactions between the electron-spins of erbium ions are expected to induce faster decoherence due to spectral diffusion (SD) [21]. Here we use pulsed electron spin resonance (ESR) spectroscopy to investigate SD in 20 ppm Er doped $CaWO_4$ in the millikelvin temperature regime. Moreover, we demonstrate a two-pulse echo coherence time of 1.3 ms for an electron-spin transition of Er at 4.4 GHz and determine that this coherence is limited by unwanted paramagnetic impurities, indicating that Er:$CaWO_4$ could be suitable for quantum information processing applications requiring large optical or microwave absorption.

II. STRUCTURE OF Er^{3+}:$CaWO_4$

Calcium tungstate is an optically-transparent crystal with tetragonal unit cell structure (space-group $I4_1/a$) and orthogonal crystal axes a, b, c. An illustration of the unit cell structure is presented in Figure 1a, which has dimensions $5.2 \times 5.2 \times 11.4$ Å parallel the crystal $a \times b \times c$ axes. Crystals grown with a natural abundance of isotopes exhibit an intrinsically low level of magnetic noise, originating almost exclusively from the nuclear spins of

* patrice.bertet@cea.fr;

a) These authors contributed equally to this work.

the ^{183}W isotope. This isotope has a natural abundance of 14 % and a nuclear spin-half moment with a relatively small gyromagnetic ratio of $\gamma_W/2\pi = 1.8$ MHz/T. For this reason $CaWO_4$ is considered one of the best candidate hosts for quantum information processing amongst thousands of known materials [20, 22].

In the crystalline matrix, the Er^{3+} ions substitutionally replace Ca^{2+} ions with additional long-range charge compensation [23]. The electrostatic interaction between the Er ions and the $CaWO_4$ matrix lifts the 16-fold degeneracy of the $J = 15/2$ electronic ground state of trivalent erbium, leading to eight pairs of degenerate electronic sub-levels known as Kramers doublets. Each doublet forms an effective spin-1/2 system and only the lowest energy Kramers doublet is populated at millikelvin temperatures. In the presence of an applied magnetic field B_0, this effective electron-spin shows a strongly anisotropic Zeeman effect, characterized by the Hamiltonian:

$$H_Z = \mu_B \, \mathbf{S} \cdot \mathbf{g} \cdot \mathbf{B_0}.$$

Here μ_B is the Bohr-magneton and $\mathbf{g}$ is the g-tensor whose symmetry mirrors the tetragonal S_4 point-group symmetry of the crystal electric-field at the location of the Er ion [24].

$$\mathbf{g} = \begin{bmatrix} 8.38 & 0 & 0 \\ 0 & 8.38 & 0 \\ 0 & 0 & 1.247 \end{bmatrix}_{(a,b,c)}$$

Additionally, 23 % of Er ions belong to the ^{167}Er isotope which has non-zero nuclear-spin $\mathbf{I} = 7/2$. For this subset of ions the magnetic-hyperfine interaction is parameterised by the hyperfine $\mathbf{A}$-tensor and therefore an additional term is required in the effective-spin Hamiltonian:

$$H_{\text{Er-167}} = \mu_B \, \mathbf{S} \cdot \mathbf{g} \cdot \mathbf{B_0} + \mathbf{S} \cdot \mathbf{A} \cdot \mathbf{I}.$$

Note that we have neglected the weak magnetic-nuclear and nuclear-quadrupole interactions in the ^{167}Er spin-Hamiltonian [25] because the additional precision awarded by these terms is not required to describe the processes studied here. Meanwhile, the $\mathbf{A}$-tensor once again reflects the symmetry of the $CaWO_4$ matrix with $A_{aa} = A_{bb} = -873$ MHz, $A_{cc} = -130$ MHz and the Hamiltonian $H_{\text{Er-167}}$ yields a total of 16 energy levels. The energy level diagrams of both H_Z and $H_{\text{Er-167}}$ are presented in the lower panel of Figure 2 for small magnetic fields applied perpendicular to the crystal c-axis.

III. EXPERIMENTAL SETUP

For these measurements we use an ESR spectrometer comprised of a thin-film superconducting resonator and Josephson Traveling Wave Parametric Amplifier (JTWPA) [26]. Such spectrometers have been described

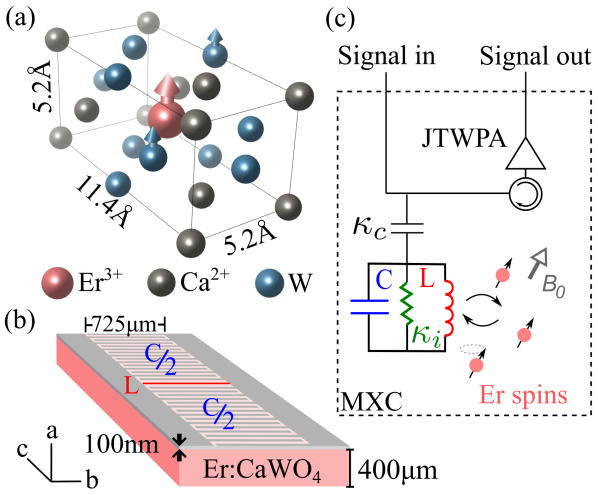

Figure 1. Experimental setup. (a) Unit cell of $CaWO_4$ showing a central Er dopant. Oxygen atoms removed for clarity (b) 3D perspective view of Er^{3+} : $CaWO_4$ crystal, showing the thin-film Nb resonator patterned on the surface. Crystal axes relevant to sub-figures (a) and (b) are shown in bottom left corner. (c) Experimental ESR setup, comprising of the resonator and JTWPA.

in detail in refs [27, 28] and achieve sensitivities as high as 12 spins/$\sqrt{\text{Hz}}$ for detecting two-pulse (Hahn) echoes originating from donors in silicon at mK temperatures [13]. This high sensitivity is due to the very low output noise, which is dominated by quantum fluctuations of the microwave field with little contribution from thermal photons at millikelvin temperatures. A 3D perspective representation of the sample studied here is shown in Fig. 1 (b). The circuit is etched into a 100 nm Nb layer sputtered directly on the surface of the $CaWO_4$ crystal, which was grown by Scientific Materials Corp. and has dimensions $0.4 \times 3 \times 6$ mm parallel to the $a \times b \times c$ axes of the crystal. The superconducting LC resonator comprises 15 interdigitated fingers (the capacitor) on either side of the 725 μm $\times$ 5 μm wire (the inductor).

The frequency of the fundamental resonator mode is $\omega_r/2\pi = 4.37$ GHz in the absence of a magnetic field, with a quality factor $Q = 8 \cdot 10^3$. The resonator Q is determined by the coupling rate to the measurement line $\kappa_C = 3 \cdot 10^6 \, s^{-1}$ and the internal energy loss rate $\kappa_i = 5 \cdot 10^5 \, s^{-1}$. For these experiments a DC magnetic field B_0 is applied parallel to the sample surface in the direction of the inductance wire (the crystal b-axis). Precision alignment of the magnetic field with respect to the crystal surface is important for minimising the internal loss rate κ_i because field penetration into the superconducting thin-film generates magnetic vortices; a well-known microwave loss channel [29].

To achieve this precision alignment, the sample is enclosed within a small copper box and mounted onto two copper-beryllium actuators from Attocube, comprising a goniometer and rotator. These are inserted into a set

of two Helmholtz coils, and thermally anchored to the mixing chamber (MXC) of a dilution refrigerator. While the actuators precisely orient the sample with respect to the applied magnetic field, they also create a weak thermal bridge due to the separation of metallic components by their piezo-electric elements and therefore additional copper-braiding is used between the sample-box and MXC assembly to maintain good thermal conductivity.

Erbium electron-spin transitions are excited with microwave signals sent from a heavily attenuated (50 dB) input line. The transmitted microwave signal, together with the signal emitted by the spin ensemble, is then amplified by the JTWPA (see Fig. 1b). Further microwave amplification takes place at 4K using a high electron mobility transistor (HEMT) and at room temperature using low-noise semiconductor amplifiers.

IV. ESR SPECTROSCOPY

This crystal demonstrates a rich ESR spectrum due to the existence of several Er isotopes in natural abundance. Shown in Figure 2, the microwave transmission spectrum is measured as a function of magnetic field applied along the crystal b-axis. Note that this spectrum was recorded at an elevated temperature of 100 mK in order to populate all the hyperfine levels of ^{167}Er.

As stated previously, however, most isotopes of Er have no nuclear spin and the largest anti-crossing at 37 mT is associated with the high concentration of $I = 0$ erbium isotopes; predominantly ^{166}Er, ^{168}Er and ^{170}Er. Here the cooperativity C between the resonator and the spin-ensemble is large ($C \approx 50$) due to the high spin density. Unfortunately, this high density of spins also gives rise to large instantaneous diffusion (ID), making it difficult to measure SD using the $I = 0$ transition (see Sup. Mat. Section I). To avoid this technical limitation, we instead focus on the low-density ^{167}Er isotope, which exhibits 16 hyperfine levels. The ESR-allowed $\Delta m_I = 0$ transitions between these levels are labelled in Fig. 2 according to their nuclear-spin projection $|m_I\rangle$. The 8 corresponding solid red lines indicate the values of B_0 for which the ESR frequencies of ^{167}Er are equal to ω_r, both experimentally (Fig. 2 Top) and theoretically (Fig. 2 Bottom). Avoided level crossings are observed in the spectrum at these field values, which is consistent with high-cooperativity between the resonator and each transition [30, 31]. Additionally, the five avoided level crossings observed in the spectrum above 38 mT are attributed to Yb impurities. The large anti-crossing at 80 mT is attributed to the $I = 0$ Yb isotopes, comprising of all the even-numbered isotopes between ^{168}Yb and ^{176}Yb.

V. SPECTRAL DIFFUSION MODEL

We use both two-pulse echoes (2PE) and three-pulse echoes (3PE) to elucidate the dynamic interactions which cause SD within the $m_I = |+3/2\rangle$ spin-ensemble of the ^{167}Er isotope. Here the 2PE consists of a $\pi/2$-pulse followed by a π-pulse at time delay τ, while the 3PE consist of three $\pi/2$ pulses with separations τ and T_W between pulses 1-2 and 2-3, respectively. The 2PE and 3PE data yield complementary information, and were first used in the 1960's by Mims, Nasau and McGee to study SD of paramagnetic rare-earth-ion impurities [32].

Since then, the theory of spectral diffusion has evolved considerably, and here we fit the 2PE and 3PE data using the uncorrelated-sudden-jump model first described by Hu and Hartmann in 1974 [33]. This model is known to yield accurate fits of optical 2PE and 3PE data in rare-earth-ion doped materials [34] and relies on four key assumptions:

1) The subset of the $m_I = |+3/2\rangle$ transition under investigation (the excited spins) are sufficiently isolated from each other such that they do not contribute to SD.

2) SD is instead caused exclusively by the magnetic dipole interaction with other denser baths of perturbing spins.

3) These perturbing spins are randomly located within the crystal matrix and exhibit only two energy configurations. i.e: a Spin-1/2 system

4) Spin-flips within the baths of perturbing spins are uncorrelated and so each flip is treated independently.

To describe explicitly this model of SD we utilise the formalism first introduced by Bai and Fayer [35] and later summarised by Bottger et. al. in a single equation suitable for both 2P- and 3P-echoes [34]. From this model, we derive a similar echo amplitude decay A_E as a function of the inter-pulse delays, extended to account for several species S of perturbating spins:

$$\mathrm{A}_E = \mathrm{V}_{eseem} \cdot \mathrm{A}_0 \exp\left(-2\pi\Gamma_{eff}\tau\right) \exp\left(\frac{-T_W}{T_1}\right) \quad (1)$$

$$\Gamma_{eff} = \Gamma_0 + \sum_S \frac{\Gamma^S_{\mathrm{SD}}}{2}\left\{R^S\tau + 1 - \exp\left(-R^S T_W\right)\right\}. \quad (2)$$

Here A_0 represents the limiting echo amplitude at zero delay and $\mathrm{V}_{eseem}(\tau, T_W)$ corresponds to the Electron Spin Echo Envelope Modulation (ESEEM) caused by the magnetic dipole-dipole interaction of the Er electron-spins and the proximal ^{183}W nuclear-spins. This is a well defined temporal modulation that depends only on the orientation and magnitude of the applied magnetic field, and has already been determined experimentally for the $m_I = |+3/2\rangle$ electron-spin transition studied here [36].

Meanwhile, the decaying component of the echo signal contains the coefficients Γ_0, Γ^S_{SD}, R^S and T_1. The coefficient Γ_0 represents decoherence processes which occur

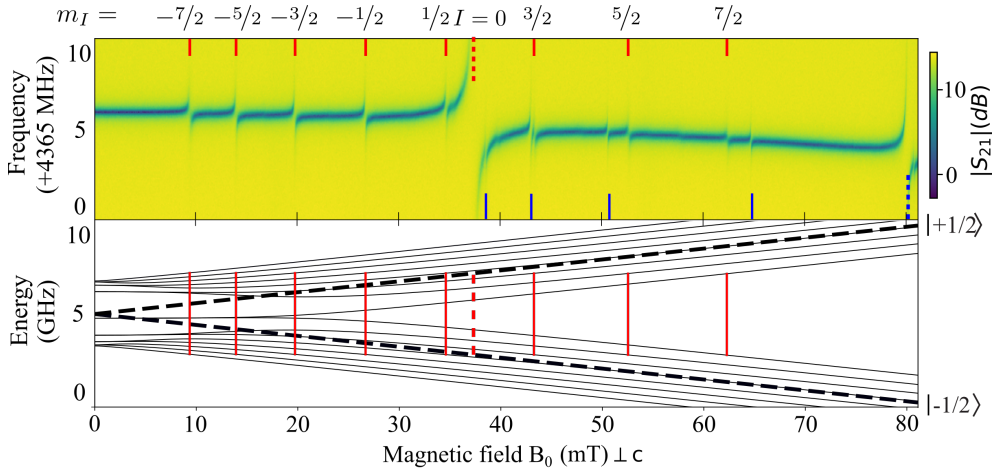

Figure 2. *Top:* ESR spectrum measured at 100 mK. At this temperature all 8 ESR transitions of ^{167}Er are populated, and these are labelled and indicated with vertical red lines at the top of the spectrum. The $m_I = +3/2$ transition studied here is just right of the large Er $I = 0$ transition, marked by vertical red dashes. Five additional ESR transitions of Yb are indicated with vertical blue lines at the bottom of the spectrum. The Yb $I = 0$ transition at 80 mT (blue dashed line) is particularly important due to its SD contribution at low temperatures. *Bottom:* Energy level diagram of ^{167}Er (solid black lines) and of Er $I = 0$ (black dashed lines). The energy levels of ^{167}Er are designated by spin-state projections $|m_S, m_I\rangle$ with the two m_S multiplets labelled on the right. The ESR transitions of Er identified in the spectrum above are marked correspondingly in red.

on faster timescales than the measurement and instantaneous diffusion (ID) caused by the microwave excitation pulses. This is equivalent to the homogeneous linewidth of a single spin transition in the absence of spectral diffusion. Conversely, $\Gamma^S_{\rm SD}$ and R^S describe the spectral diffusion which occurs during the delays τ and T_W due to spin species S. More specifically, R^S represents the average spin-flip rate and $\Gamma^S_{\rm SD}$ is the full-width-half-maximum (FWHM) contribution to the dynamic distribution of transition frequencies within the $m_I = |+3/2\rangle$ sub-ensemble.

Indeed, any paramagnetic species or ESR transition that exhibits ppm or higher concentration can contribute significant amounts of spectral diffusion, and therefore it is important to identify all paramagnetic impurities in the material and determine their concentration. Initially, this was attempted via magnetic-rotation-spectroscopy (Sup. Mat. Section II) combined with numerical spin-resonator coupling estimates (Sup. Mat. Section III) which identified both Yb^{3+} and Mn^{2+} impurities.

However, our quantum-limited spectrometer was not able to detect paramagnetic impurities with small g-factors or long spin-lattice relaxation rates due to the limited magnetic field (400 mT) and temperature (600 mK). Thus a piece of the $CaWO_4$ boule was submitted for inductively-coupled-plasma mass-spectrometry (ICP-MS) analysis and the results are presented in Table I [37].

Mass-spectrometry allowed for the concentration of the previously-identified Er, Yb and Mn impurities to be determined with high precision and three additional rare-earth-ion impurities were also identified in the crystal at lower concentrations.

Element	Mn	Ce	Nd	Gd	Er	Yb
Conc. ($\mu g/g$)	0.542	0.424	0.211	0.066	13.292	8.516
Conc. (ppm)	2.840	0.871	0.421	0.120	22.88	14.17

Table I. Calcium-relative impurity concentrations detected in a dissolved (aqueous) sample of the $CaWO_4$ boule, represented by relative mass concentration (top row) and the equivalent relative doping concentration (bottom row). This measurement was performed at the European Centre for Environmental Geoscience Research and Teaching using a Perkin Elmer NexION 300X mass-spectrometer.

The two ESR transitions with the greatest absorption; the $I = 0$ Er and Yb transitions, were thereby included in the SD analysis. For each transition (i.e: species) S, the linewidth $\Gamma^S_{\rm SD}$ is proportional to the number of spins which can undergo spin-flip, and the expected temperature dependence is described by Boltzmann statistics [34]:

$$\Gamma^S_{\rm SD}(T) = \Gamma^S_{\rm max}\mathrm{sech}^2\left(\frac{g_S\mu_B B_0}{2kT_B}\right), \qquad (3)$$

where k is the Boltzmann constant, T_B is the electron-spin bath temperature and g_S is the g-factor of the electron-spin transition in the direction of the applied field B_0. The constant $\Gamma^S_{\rm max}$ is the maximum dynamic linewidth contribution from species S. In the high-temperature limit $\Gamma^S_{\rm SD}$ approaches $\Gamma^S_{\rm max}$ asymptotically, as the spin-down and spin-up populations of species S

equalize and the magnetic-dipole interaction with the $m_I = |+3/2\rangle$ sub-ensemble is maximised. Meanwhile, R^S is the associated rate of spin-flips (the sum of upward and and downward spin-flips) which is also temperature dependent and has two contributions for the studied temperature range. The first is due to the spin flip-flops, which follows the same temperature dependence as in Eq. 3. The second is the spin-lattice (phonon) interaction resonant with the spin-transition frequency $\omega_S = \mu_B g_S B_0/\hbar$, yielding the following equation [34, 38]:

$$R^S(T) = \alpha_{ff}\frac{{g_{S\perp}}^4 n_S^2}{\Gamma_S}\mathrm{sech}^2\left(\frac{g_S\mu_B B_0}{2kT_B}\right) + \alpha_{ph} g_S^3 B_0^5 \coth\left(\frac{g_S\mu_B B_0}{2kT_B}\right). \quad (4)$$

Here α_{ff} and α_{ph} represent scaling constants of the flip-flop and spin-lattice interactions respectively, and it is assumed they do not vary between different paramagnetic species in the crystal. Meanwhile, n_S represents the density of species S and Γ_S the FWHM of the inhomogeneously broadened ESR absorption line, which can depend on both the magnitude and direction of the applied magnetic field. Additionally, g_S represents the g-factor in the direction of the applied field, while $g_{S\perp}$ is the g-factor in the direction orthogonal to the c-axis of the crystal. Note that the flip-flop rate is only sensitive to the components of the g-tensor perpendicular to the direction of the applied field [39]. Here the magnetic field is applied along the b-axis of the crystal, so this coupling depends on the spectroscopic splitting factors in the directions of both the a- and c-axes, namely $g_\perp$ and $g_\parallel$. As $g_\parallel \ll g_\perp$ for both erbium and ytterbium, we approximate this angular dependence using only $g_\perp$ in the expression for the flip-flop rate.

In the limit $T_W = 0$, the effective linewidth presented in Eq (2) simplifies to $\Gamma_0 + \tau/2\sum\Gamma^S_{\mathrm{SD}}R^S$. Thus, it is impossible to obtain independent values for Γ_{SD} and R with only 2PE measurements, due to the multiplicative relationship between these two parameters. For this reason 3PE measurements are necessary to obtain an independent fit of Γ_{SD} and R.

VI. ENSEMBLE COUPLING MEASUREMENTS

To accurately fit the temperature dependence of Γ_{SD} and R it is also important to know the temperature T_B of the electron-spin bath, as this can be higher than the temperature of the mixing chamber (T_{MXC}) due to limited thermal conduction. Here we independently determine T_B as a function of T_{MXC} by evaluating the coupling of the $m_I = |+3/2\rangle$ sub-ensemble to the resonator at each measured temperature, using a well established

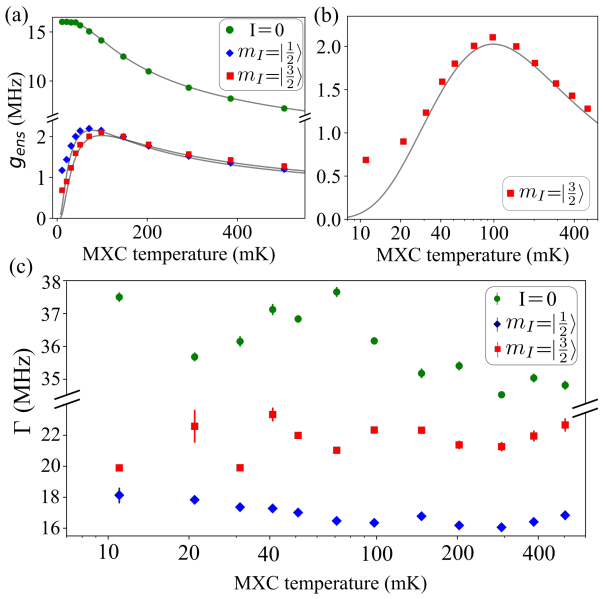

Figure 3. Ensemble coupling and inhomogeneous linewidths as a function of MXC temperature, determined using a fit to Eq. (5) for three electron-spin transitions of Er: The $I = 0$ transition (green), the $m_I = |\frac{1}{2}\rangle$ (blue) and $m_I = |\frac{3}{2}\rangle$ (red) transitions of ^{167}Er. (a) g_{ens} values extracted from the fit (coloured dots). The solid black lines show a simultaneous fit to all three g_{ens} data-sets assuming a thermal Boltzmann distribution of spin-levels. (b) Same data as in subplot (a) for the $m_I = |\frac{3}{2}\rangle$ transition, presented with a logarithmic temperature scale. (c) Inhomogeneous linewidths Γ extracted from the same fitting as in subfigure (a) presented with a logarithmic temperature scale. Here a negligible temperature dependence is observed for all three transitions, consistent with the observation that inhomogeneous broadening of paramagnetic impurities is dominated by electrostatic perturbations in $CaWO_4$ [40, 41].

complex transmission formula [42]:

$$S_{21}(\omega) = 1 - \frac{\kappa_C}{2i(\omega-\omega_r) + \kappa_T + \sum_S \frac{2(2\pi g^S_{ens})^2}{i(\omega-\omega_S)+\pi\Gamma_S}}, \quad (5)$$

where g^S_{ens} is the temperature-dependent ensemble coupling between the electron-spin species S and the resonator and the other variables are as previously defined. Example fits of g^S_{ens} and Γ_S are presented in section III of the supplementary materials for several Er and Yb transitions. Figure 3 presents the results of this fitting as a function of T_{MXC} for three of the electron-spin transitions presented in Fig. 2; the $|+1/2\rangle$, $I = 0$ and $|+3/2\rangle$ transitions.

Noting that g^S_{ens} is proportional to the square-root of the electron-spin polarisation of species S [42], we can directly compare the fitted ensemble-coupling at each measured temperature with the expected temperature dependence, assuming the Er electron- and nuclear-spin populations thermalise to T_{MXC} according to Boltz-

mann statistics (refer to Sup. Mat. Section IV for more detail).

Indeed, the solid black lines in Fig. 3a represent a simultaneous fit to g^S_{ens} for all three transitions. The only free parameter in this fit is the total Er concentration, which yields $2 \cdot 10^{17}$ spins/cm^3, equivalent to 18 ppm substitutional doping. This is consistent with the concentration determined by mass-spectrometry (Table I) which was used for the analysis of the 3PE measurements (Sup. Mat. Section V).

Figure 3b presents an enlarged view of the ensemble-coupling data and fit for the $m_I = |+3/2\rangle$ transition. This transition was chosen to probe the spin-temperature below 100 mK because the nuclear-spin distribution of ^{167}Er is considerably more sensitive to heating in this temperature region than the electron-spin distribution of the $I = 0$ Er isotopes, shown by the green curve in Fig. 3a. Moreover, we assume that this measurement of the hyperfine level temperature of ^{167}Er accurately determines the electron-spin bath temperature (T_B) of all paramagnetic impurities in the sample because of the strong hyperfine coupling between the electronic and nuclear spin of ^{167}Er, which keeps both spin baths isothermal. In particular, the fit to the data in Fig. 3b suggests that T_B is well approximated by T_{MXC} above 30 mK. Below this MXC temperature, however, we infer that poor thermal conduction combined with some heating at-or-near the location of the sample leads to an elevated bath temperature with $T_B = 23 \pm 2$ mK at $T_{MXC} = 11$ mK and $T_B = 27 \pm 2$ mK when $T_{MXC} = 21$ mK.

Both the excess heating and poor conductivity are likely caused by the piezo-electric actuators that precisely align the sample in the applied magnetic field. The issue of poor thermal conductivity was mentioned previously in Section II and the frictional 'stick-slip' mechanism which moves the actuators could potentially be a heat-source even during static (non-moving) operation [43]. This is possible if vibrations from the pulse-tube cooler couple to the loose frictional surfaces within the actuators, which are required for precise displacement. Indeed, thermal excursions up to 100 mK were observed when the actuators are actively displaced using a voltage signal, and this temperature rise is attributed to frictional heating.

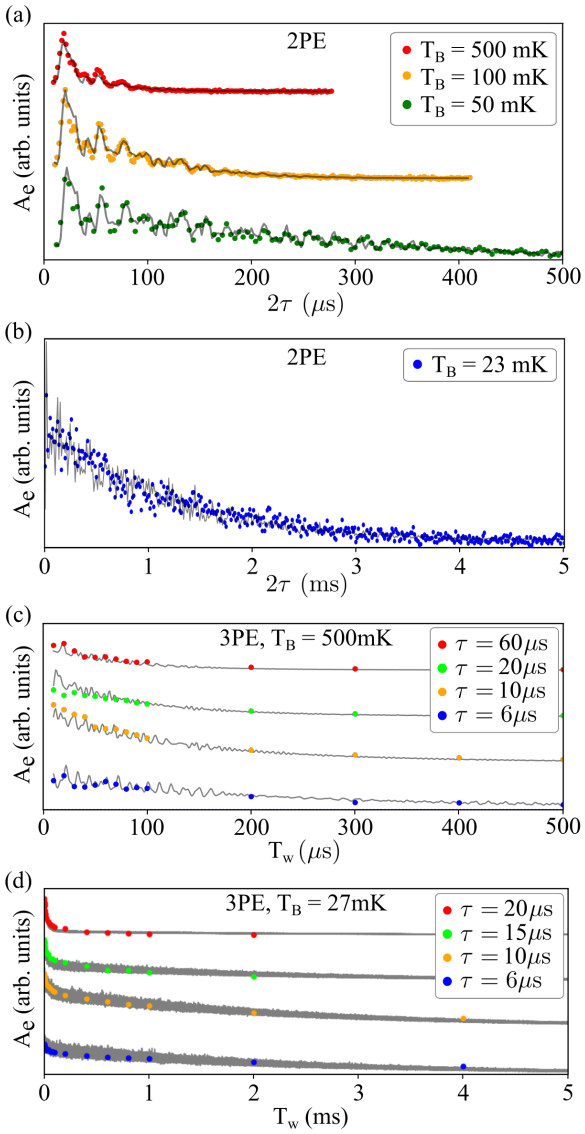

Figure 4. Two- and three-pulse echo decay curves (coloured dots) measured as a function of delay times τ or T_W and their respective fits (grey solid curves). (a) Waterfall plot of two-pulse echo decay-curves measured in the temperature range of 50-500 mK. (b) Two-pulse echo measurement recorded at $T_B = 23$ mK; the lowest achievable spin-bath temperature for the experiments performed here. (c) Waterfall plot of three-pulse echo decay curves measured at $T_B = 530$ mK as a function of both τ and T_W time-delays. (d) Waterfall plot of three-pulse echo decay curves measured at $T_B = 27$ mK.

VII. ECHO MEASUREMENTS

As mentioned at the beginning of Section V, 2PE and 3PE measurements were recorded at various spin-bath temperatures T_B to determine the SD parameters $\Gamma^S_{\rm SD}$ and R^S. A selection of these measurements is presented in Figure 4. To accurately determine the echo decay rates, it was necessary to fit the large ESEEM modulation depths observed in Fig. 4a and b. Fortunately, the ESEEM parameters have already been measured and published for the sample and experimental configuration used here [36].

For the 3PE measurements, up-to ten decay curves were taken at five different temperatures as a function of T_W, with fixed τ ranging from 6 μs to 96 μs. These small values of τ were chosen for the 3PE measurements because they allow for accurate estimates of the rapid SD at higher temperatures. An example set of 3PE

curves recorded at 530 mK and 27 mK are presented in sub-figures 4c and 4d, respectively. ESEEM is also present and simulated for the 3PE decay-curves, however, the data was recorded with large T_W-spacings and so the fitted curves in grey show an under-sampling of the modulation.

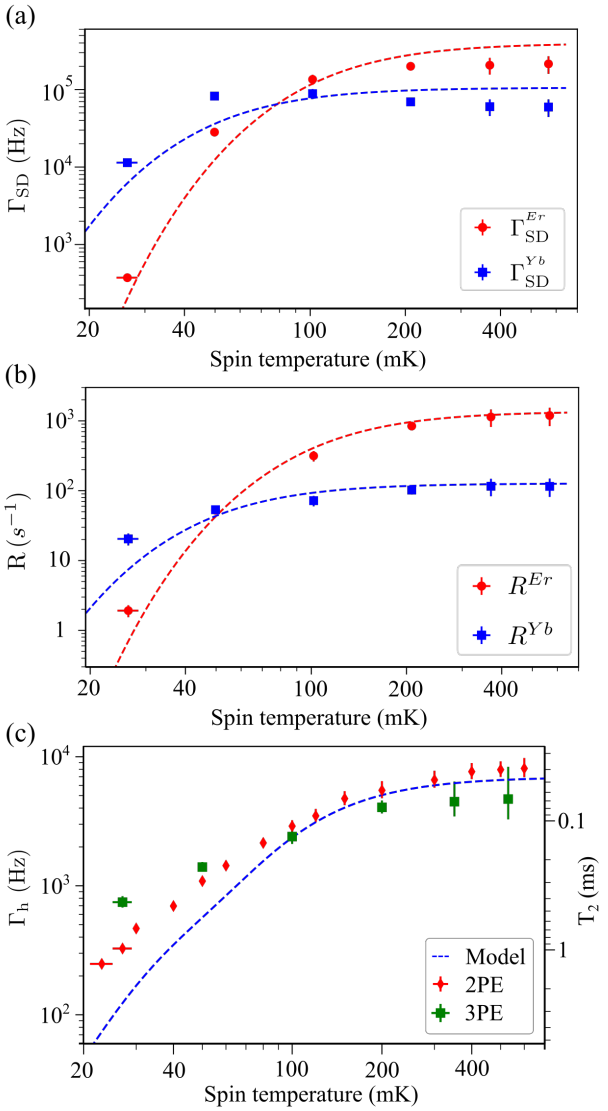

Figure 5. Spectral diffusion and decoherence rates. (a) Linewidth Γ_{SD} and (b) spin-flip rates R^S extracted from 3PE fits to Eq.(1) for six temperatures and two spin species. Y-errors shows standard error in the fit. Red(blue) dashed lines in (a) and (b) represent fits to Eq. (3) and (4) for Er(Yb), respectively. (c) Extracted coherence time T_2 (Right hand side) and equivalent effective decoherence rate $\Gamma_h = 1/\pi T_2$ (left hand side) from the 2PE data (red) and the 3PE data (green). The decoherence model (in blue) takes into account the SD parameters extracted from the 3PE measurements, the ID of the $m_I = |+3/2\rangle$ transition and the dephasing caused by the unpolarised ^{183}W nuclear spin bath.

As mentioned previously, we rely on 3PE data to determine R and Γ_{SD} at each measured temperature because 2PE measurements cannot be used to fit these these two parameters independently. For this fitting we also consider only the flip-flop contribution of $R^S(T)$ and the relative concentration of Er and Yb impurities. The result of this fitting is presented in Figures 5a and 5b, and the details of the fitting process are presented in section V of the supplementary materials. For both the 2PE and 3PE measurements it is then possible to define a coherence time

$$T_2 = \frac{-a + \sqrt{a^2 + 2b/\pi}}{b}. \tag{6}$$

Here $a = \Gamma_0$ and $b = \frac{1}{2}\sum_S \Gamma_{SD}^S R^S$. These two parameters arise from the quadratic exponent $\Gamma_{eff}\tau = a\tau + b\tau^2$ presented in Eq. (2) when $T_W = 0$. For both the 2PE and 3PE measurements, this value of T_2 represents the time 2τ when the echo has decayed to e^{-1} of its initial amplitude (in the limit $T_W = 0$ for 3PE measurements) and is presented in Fig. 5c.

Above 100 mK the value of T_2 inferred from either 2PE or 3PE measurements agree within error. However, they diverge below this temperature due to the difficulty in determining T_2 accurately using 3PE measurements when $T_2 \gg \tau$. Instead, the long tail of the T_W-dependent decay visible in Figs. 4c and 4d is sensitive to spectral-diffusion processes that occur on timescales much longer than T_2. For this reason we rely solely on the 2PE fit to determine T_2 at the lowest spin-bath temperatures, and we observe a maximum value of $T_2 = 1.3 \pm 0.1$ ms at $T_B = 23$ mK.

VIII. ANALYSIS

Figures 5a and 5b illustrate the large decrease in Γ_{SD} and R with decreasing temperature for both the Er and Yb spins. We attribute this to a reduction in the electron-spin flip-flop rate as a consequence of thermal polarisation of the spin populations. Indeed, our a-priori neglect of spin-lattice contribution in our SD analysis (Sup. Mat. Section V) is justified by the rapid spin-flip rates observed across the studied temperature range. For instance, R^{Er} is orders-of-magnitude greater than the spin-lattice relaxation rate $T_1^{-1} = 0.01\,\mathrm{s}^{-1}$ estimated from previous measurements of spin-lattice relaxation in Er:$CaWO_4$ at 7.88 GHz and 500 mK [19], given the $g_S^3 B_0^5$ scaling presented in Equation 4.

While flip-flops within the Er electronic-spin bath are clearly the dominant source of SD at high temperature, the Yb electron-spins contribute most to SD at $T_B = 23$ mK. This occurs because the Yb spins are less thermally polarised as a consequence of their smaller g-factor, even though the Yb spin-bath is less dense than the Er bath. Moreover, the total experimental contribution to SD from both the Er and Yb spins at the lowest temperature is significantly greater than the expected

contribution shown by the dashed-line fits in Figs. 5a & 5b.

This discrepancy is also present in the decoherence-rate model presented in Figure 5c. This model is detailed in Section VI of the supplementary materials and takes into account the expected contribution of the temperature-dependent instantaneous diffusion due to pulse-excitation in addition to the dephasing caused by the ^{183}W nuclear spin bath. Here the instantaneous diffusion contribution is temperature-dependent due to the thermal population density of the $m_I = |+3/2\rangle$ hyperfine state. Using the method described in Refs [44, 45] we estimate minimum and maximum contributions of 51 Hz at 23 mK and 630 Hz at 530 mK, respectively. The temperature-independent dephasing caused by the unpolarised ^{183}W nuclear spin bath contributes only 12 Hz; a value derived from the cluster-correlation expansion estimate of T_2 determined by Le Dantec et. al. [19] for the Er electron-spin transition in $CaWO_4$.

The remaining discrepancy can have two possible origins. The first is that the uncorrelated-sudden-jump model presented in Section V makes the incorrect assumption that all spin-flips are uncorrelated in this system. Although this is valid for spin-flips driven predominantly by spin-lattice relaxation, as has been the case in previous applications of this model [34], there is an inherent correlation between spins-flips when they are driven by flip-flops. While the derivation of a 'correlated-sudden-jump' model which accounts for this discrepancy is beyond the scope of this work, it would be possible to investigate this issue further by simulating flip-flops of the paramagnetic spin baths using the cluster-correlation expansion approach [46, 47].

The second possibility is that one or more additional electron-spin species are contributing significantly to SD at low temperatures, consistent with the observation of additional impurities in the mass-spectrum (Table I). One likely candidate species is Mn^{2+}; the third most abundant impurity in the crystal at a relative concentration of 2.8 ppm. With a g-factor of 2, manganese is weakly polarised at 23 mK and an estimate of the SD contribution were not undertaken here due to the complex electronic level structure in mT fields. [48].

IX. CONCLUSION

Here we demonstrated an electron-spin coherence time exceeding 1 millisecond in 20 ppm doped Er^{3+}:$CaWO_4$, achieved by cooling the electronic spin bath to 23 mK and thereby significantly reducing the electron-spin flip-flop rate of both the Er and Yb impurities.

Further enhancements in spin-coherence could be achieved by chemically purifying the host matrix or improving the thermal spin-polarisation. For instance, increasing the resonator frequency from 4.4 to 8 gigahertz would significantly improve thermal-polarisation while maintaining compatibility with superconducting microwave circuits that typically operate in the 4-8 GHz band. In this situation one would expect the SD contribution of the Er and Yb spins to be reduced by factors of approximately 10^3 and 10^2 respectively, at a spin-bath temperature of 23 mK.

Chemical purification is also an important avenue to pursue because the smaller g-factors of non-erbium impurities will generally lead to significant SD contributions at low temperatures. Indeed, ytterbium alone presents an SD contribution 320 times greater than erbium at 4.4 GHz and 23 mK. Reducing the Yb concentration to the ppb level observed in chemically purified $CaWO_4$ would reduce this contribution by seven orders of magnitude, assuming the inhomogeneous spin-transition linewidth remains largely unchanged.

Such improvements could result in coherence-times approaching the nuclear-spin-limited T_2 of 27 milliseconds [19], while maintaining ppm Er concentrations.

Acknowledgements

We acknowledge technical support from P. Sénat, D. Duet, P.-F. Orfila, and S. Delprat, and we are grateful for fruitful discussions within the Quantronics group. We acknowledge IARPA and Lincoln Labs for providing the Josephson traveling-wave parametric amplifier.

This project has received funding from the European Union's Horizon 2020 research and innovation program under Marie Sklodowska-Curie grant agreement no. 765267 (QuSCO) and no. 792727 (SMERC). E.F. acknowledges support from the Agence Nationale de la Recherche (ANR) grant DARKWADOR:ANR-19-CE47-0004. We acknowledge support from the ANR through the Chaire Industrielle NASNIQ under contract ANR-17-CHIN-0001 cofunded by Atos and through the project MIRESPIN under contract ANR-19-CE47-0011 and of the Region Ile-de-France through the DIM SIRTEQ (REIMIC project). We acknowledge support of the AIDAS virtual joint laboratory. R.B.L. was supported by Hong Kong Research Grants Council - General Research Fund (Project 14302121). S.L. was supported by the Impact Postdoctoral Fellowship of CUHK. S.B. thanks the support of the CNRS research infrastructure RENARD (FR 3443)

[1] Zhong, M. *et al.* Optically addressable nuclear spins in a solid with a six-hour coherence time. *Nature* **517**, 177–180 (2015). URL http://dx.doi.org/10.1038/nature14025.

[2] Holzäpfel, A. *et al.* Optical storage for 0.53 s in a solid-state atomic frequency comb memory using dynamical decoupling. *New Journal of Physics* **22**, 063009 (2020). URL https://iopscience.iop.org/article/10.1088/1367-2630/ab8aachttps://iopscience.iop.org/article/10.1088/1367-2630/ab8aac/meta. 1910.08009.

[3] Longdell, J. J., Fraval, E., Sellars, M. J. & Manson, N. B. Stopped Light with Storage Times Greater than One Second Using Electromagnetically Induced Transparency in a Solid. *Physical Review Letters* **95**, 063601 (2005). URL http://link.aps.org/doi/10.1103/PhysRevLett.95.063601.

[4] Rančić, M., Hedges, M. P., Ahlefeldt, R. L. & Sellars, M. J. Coherence time of over a second in a telecom-compatible quantum memory storage material. *Nature Physics* **14**, 50–54 (2018). URL http://www.nature.com/doifinder/10.1038/nphys4254.

[5] Hedges, M. P., Longdell, J. J., Li, Y. & Sellars, M. J. Efficient quantum memory for light. *Nature* **465**, 1052–1056 (2010). URL http://www.ncbi.nlm.nih.gov/pubmed/20577210http://dx.doi.org/10.1038/nature09081.

[6] Dajczgewand, J., Le Gouët, J.-L., Louchet-Chauvet, A. & Chanelière, T. Large efficiency at telecom wavelength for optical quantum memories. *Optics Letters* **39**, 2711 (2014). URL https://www.osapublishing.org/abstract.cfm?URI=ol-39-9-2711.

[7] Sabooni, M., Li, Q., Kröll, S. & Rippe, L. Efficient Quantum Memory Using a Weakly Absorbing Sample. *Physical Review Letters* **110**, 133604 (2013). URL http://link.aps.org/doi/10.1103/PhysRevLett.110.133604.

[8] Bartholomew, J. G. *et al.* On-chip coherent microwave-to-optical transduction mediated by ytterbium in YVO4. *Nature Communications* **11**, 1–6 (2020). URL https://www.nature.com/articles/s41467-020-16996-x. 1912.03671.

[9] Fernandez-Gonzalvo, X., Horvath, S. P., Chen, Y. H. & Longdell, J. J. Cavity-enhanced Raman heterodyne spectroscopy in Er^{3+}:Y_2SiO_5 for microwave to optical signal conversion. *Physical Review A* **100**, 033807 (2019). 1712.07735.

[10] Grezes, C. *et al.* Towards a spin-ensemble quantum memory for superconducting qubits (2016). 1510.06565.

[11] Sigillito, A. J. *et al.* Fast, low-power manipulation of spin ensembles in superconducting microresonators. *Applied Physics Letters* **104**, 222407 (2014). URL http://aip.scitation.org/doi/10.1063/1.4881613. 1403.0018.

[12] Grèzes, C. *Towards a spin ensemble quantum memory for superconducting qubits*. Phd thesis, Universite Paris-Saclay (2015).

[13] Ranjan, V. *et al.* Electron spin resonance spectroscopy with femtoliter detection volume. *Applied Physics Letters* **116**, 184002 (2020). URL https://aip.scitation.org/doi/abs/10.1063/5.0004322.

[14] Probst, S., Rotzinger, H., Ustinov, A. V. & Bushev, P. A. Microwave multimode memory with an erbium spin ensemble. *Physical Review B - Condensed Matter and Materials Physics* **92**, 014421 (2015). URL https://journals.aps.org/prb/abstract/10.1103/PhysRevB.92.014421. 1501.01499.

[15] Dold, G. *milliKelvin ESR of rare-earth doped crystals using superconducting resonators*. Phd thesis, University College London (2020).

[16] Li, P. Y. *et al.* Hyperfine Structure and Coherent Dynamics of Rare-Earth Spins Explored with Electron-Nuclear Double Resonance at Subkelvin Temperatures. *Physical Review Applied* **13**, 024080 (2020). 1910.12351.

[17] Rakonjac, J. V., Chen, Y.-H., Horvath, S. P. & Longdell, J. J. Long spin coherence times in the ground state and in an optically excited state of $^{167}Er^{3+}$:Y_2SiO_5 at zero magnetic fields. *Physical Review B* 184430 (2020). URL https://journals.aps.org/prb/abstract/10.1103/PhysRevB.101.184430.

[18] Ortu, A. *et al.* Simultaneous coherence enhancement of optical and microwave transitions in solid-state electronic spins. *Nature Materials 2018 17:8* **17**, 671–675 (2018). URL https://www.nature.com/articles/s41563-018-0138-x. 1712.08615.

[19] Dantec, M. L. *et al.* Twenty-three millisecond electron spin coherence of erbium ions in a natural-abundance crystal. *Science Advances* **7**, 9786 (2021). URL https://www.science.org/doi/full/10.1126/sciadv.abj9786. 2106.14974.

[20] Kanai, S. *et al.* Generalized scaling of spin qubit coherence in over 12,000 host materials (2021). URL https://arxiv.org/abs/2102.02986v1. 2102.02986.

[21] Herzog, B. & Hahn, E. L. Transient nuclear induction and double nuclear resonance in solids. *Physical Review* **103**, 148–166 (1956).

[22] Ferrenti, A. M., de Leon, N. P., Thompson, J. D. & Cava, R. J. Identifying candidate hosts for quantum defects via data mining. *npj Computational Materials* **6**, 1–6 (2020). URL https://www.nature.com/articles/s41524-020-00391-7. 2006.14128.

[23] Kiel, A. & Mims, W. B. Electric-Field-Induced g Shifts for Loose Yb Ions in Three Scheelite Lattices. *Physical Review B* **1**, 2935–2944 (1970). URL https://link.aps.org/doi/10.1103/PhysRevB.1.2935.

[24] Bertaina, S. *et al.* Rare-earth solid-state qubits. *Nature Nanotechnology* **2**, 39–42 (2007). URL http://www.nature.com/doifinder/10.1038/nnano.2006.174http://www.nature.com/articles/nnano.2006.174.

[25] Guillot-Noël, O. *et al.* Hyperfine interaction of Er^{3+} ions in Y_2:SiO_5 : An electron paramagnetic resonance spectroscopy study. *Physical Review B* **74**, 214409 (2006). URL http://link.aps.org/doi/10.1103/PhysRevB.74.214409.

[26] Macklin, C. *et al.* A near-quantum-limited Josephson traveling-wave parametric amplifier. *Science* **350**, 307–310 (2015).

[27] Probst, S. *et al.* Inductive-detection electron-spin resonance spectroscopy with $65 spins/\sqrt{Hz}$ sen-

sitivity. *Applied Physics Letters* **111**, 202604 (2017). URL http://aip.scitation.org/doi/10.1063/1.5002540. 1708.09287.

[28] Bienfait, A. *et al.* Reaching the quantum limit of sensitivity in electron spin resonance. *Nature nanotechnology* **11**, 253–257 (2015). URL http://www.nature.com/doifinder/10.1038/nnano.2015.282. 1507.06831.

[29] Song, C. *et al.* Microwave response of vortices in superconducting thin films of Re and Al. *Physical Review B - Condensed Matter and Materials Physics* **79**, 174512 (2009). URL https://journals.aps.org/prb/abstract/10.1103/PhysRevB.79.174512. 0812.3645.

[30] Probst, S. *et al.* Anisotropic rare-earth spin ensemble strongly coupled to a superconducting resonator. *Physical review letters* **110**, 157001 (2013). URL https://link.aps.org/doi/10.1103/PhysRevLett.110.157001https://journals.aps.org/prl/abstract/10.1103/PhysRevLett.110.157001.

[31] Kubo, Y. *et al.* Strong Coupling of a Spin Ensemble to a Superconducting Resonator. *Physical Review Letters* **105**, 140502 (2010). URL https://link.aps.org/doi/10.1103/PhysRevLett.105.140502.

[32] Mims, W. B., Nassau, K. & McGee, J. D. Spectral Diffusion in Electron Resonance Lines. *Physical Review* **123**, 2059 (1961). URL https://journals.aps.org/pr/abstract/10.1103/PhysRev.123.2059.

[33] Hu, P. & Hartmann, S. R. Theory of spectral diffusion decay using an uncorrelated-sudden-jump model. *Physical Review B* **9**, 1 (1974). URL https://journals.aps.org/prb/abstract/10.1103/PhysRevB.9.1.

[34] Böttger, T., Thiel, C. W., Sun, Y. & Cone, R. L. Optical decoherence and spectral diffusion at 1.5 μm in Er^{3+}:Y_2SiO_5 versus magnetic field, temperature, and Er^{3+} concentration. *Physical Review B* **73**, 075101 (2006). URL http://link.aps.org/doi/10.1103/PhysRevB.73.075101.

[35] Bai, Y. S. & Fayer, M. D. Time scales and optical dephasing measurements: Investigation of dynamics in complex systems. *Physical Review B* **39**, 11066 (1989). URL https://journals.aps.org/prb/abstract/10.1103/PhysRevB.39.11066.

[36] Probst, S. *et al.* Hyperfine spectroscopy in a quantum-limited spectrometer. *Magnetic Resonance* **1**, 315–330 (2020). 2001.04854.

[37] Angeletti, B. & Ambrosi, J. P. European Centre for Environmental Geoscience Research and Teaching (2020). URL https://www.cerege.fr/en/analytic-facilities/la-icp-ms-platform-elemental-chemistry.

[38] Dantec, M. L. *Electron spin dynamics of erbium ions in scheelite crystals , probed with superconducting resonators at millikelvin temperatures.* Ph.D. thesis, Université Paris-Saclay (2022). URL https://tel.archives-ouvertes.fr/tel-03579857.

[39] Car, B., Veissier, L., Louchet-Chauvet, A., Le Gouët, J. L. & Chanelière, T. Optical study of the anisotropic erbium spin flip-flop dynamics. *Physical Review B* **100**, 165107 (2019). URL https://journals.aps.org/prb/abstract/10.1103/PhysRevB.100.165107. 1811.10285.

[40] Mims, W. B. & Gillen, R. Broadening of paramagnetic-resonance lines by internal electric fields. *Physical Review* **148**, 438–443 (1966). URL https://journals.aps.org/pr/abstract/10.1103/PhysRev.148.438.

[41] Baibekov, E. I. *et al.* Broadening of paramagnetic resonance lines by charged point defects in neodymium-doped scheelites. *Optics and Spectroscopy* **116**, 661–666 (2014). URL http://link.springer.com/10.1134/S0030400X1405004X.

[42] Ranjan, V. *et al.* Probing Dynamics of an Electron-Spin Ensemble via a Superconducting Resonator. *Physical Review Letters* **110**, 067004 (2013). URL https://link.aps.org/doi/10.1103/PhysRevLett.110.067004. 1208.5473.

[43] Zech, M., Schoebel, J. & Pickert, T. Stick-slip drive, especially pieze-actuated inertial drive (2019). URL https://patents.google.com/patent/US10505470B2/en.

[44] Kurshev, V. V. & Ichikawa, T. Effect of spin flip-flop on electron-spin-echo decay due to instantaneous diffusion. *Journal of Magnetic Resonance (1969)* **96**, 563–573 (1992).

[45] Tyryshkin, A. M. *et al.* Electron spin coherence exceeding seconds in high-purity silicon. *Nature Materials 2011 11:2* **11**, 143–147 (2011). URL https://www.nature.com/articles/nmat3182.

[46] Yang, W. & Liu, R. B. Quantum many-body theory of qubit decoherence in a finite-size spin bath. *Physical Review B - Condensed Matter and Materials Physics* **78**, 085315 (2008). 0806.0098.

[47] Yang, W. & Liu, R. B. Quantum many-body theory of qubit decoherence in a finite-size spin bath. II. Ensemble dynamics. *Physical Review B - Condensed Matter and Materials Physics* **79**, 115320 (2009). 0902.3055.

[48] Hempstead, C. F. & Bowers, K. D. Paramagnetic resonance of impurities in CaWO4. I. Two S-state ions. *Physical Review* **118**, 131–134 (1960).

Supplementary Materials

March 30, 2022

Section I: Measurements of Instantaneous Diffusion

Instantaneous diffusion is often not an intrinsic decoherence mechanism of the material, and is usually the result of applied microwave pulses which perturb the spins and thereby induce dephasing via the magnetic-dipole interaction between the excited spins. This phenomenon is often a significant source of dephasing for ESR transitions with very high spin densities and its contribution can be quantified by studying the coherence time of two-pulse-echoes (2PE) as a function of applied microwave pulse power. For the Er $I = 0$ transition in particular, T_2 changes drastically with applied power. This can be seen in Figure 1 (a) & (b).

Although it is possible to achieve longer coherence times in the presence of ID by reducing the applied microwave pulse power, the longest T_2 time achieved here on the Er $I = 0$ transition is only $720\mu s$, as shown in Figure 1b. This is considerably shorter than the 1.3ms measured on the $m_I = |+3/2\rangle$ sub-ensemble at the same spin-bath temperature. Figure 1c shows the relative contribution of instantaneous and spectral diffusion in this decay rate when the 2PE curves are fitted using a phenomenological spectral diffusion model based on Eq. (1) of the main text:

$$\mathrm{A}_e = \mathrm{V}_{eseem}(\tau, T_W) \cdot \mathrm{A}_0 \exp\left(-2\pi\tau\left[\Gamma_0 + \tau\Gamma_{\mathrm{SD}} R/2\right]\right)$$

Here Γ_0 demonstrates a strong dependence on pulse-power (Fig. 1c) which is consistent with ID caused by pulse-driven inter-spin interactions. However, we do not observe the expected $\sin^2\theta$ dependence with respect to applied-pulse angle θ [44, 45]. This is likely because of the spatial-inhomogeneity of the spin-resonator coupling (and hence inhomogeneity of the Rabi angle) for the micro-resonator geometry used here. Moreover, the spin-excitation volume also changes with applied microwave power which can be a confounding factor if the magnetic interactions are sufficiently long-range.

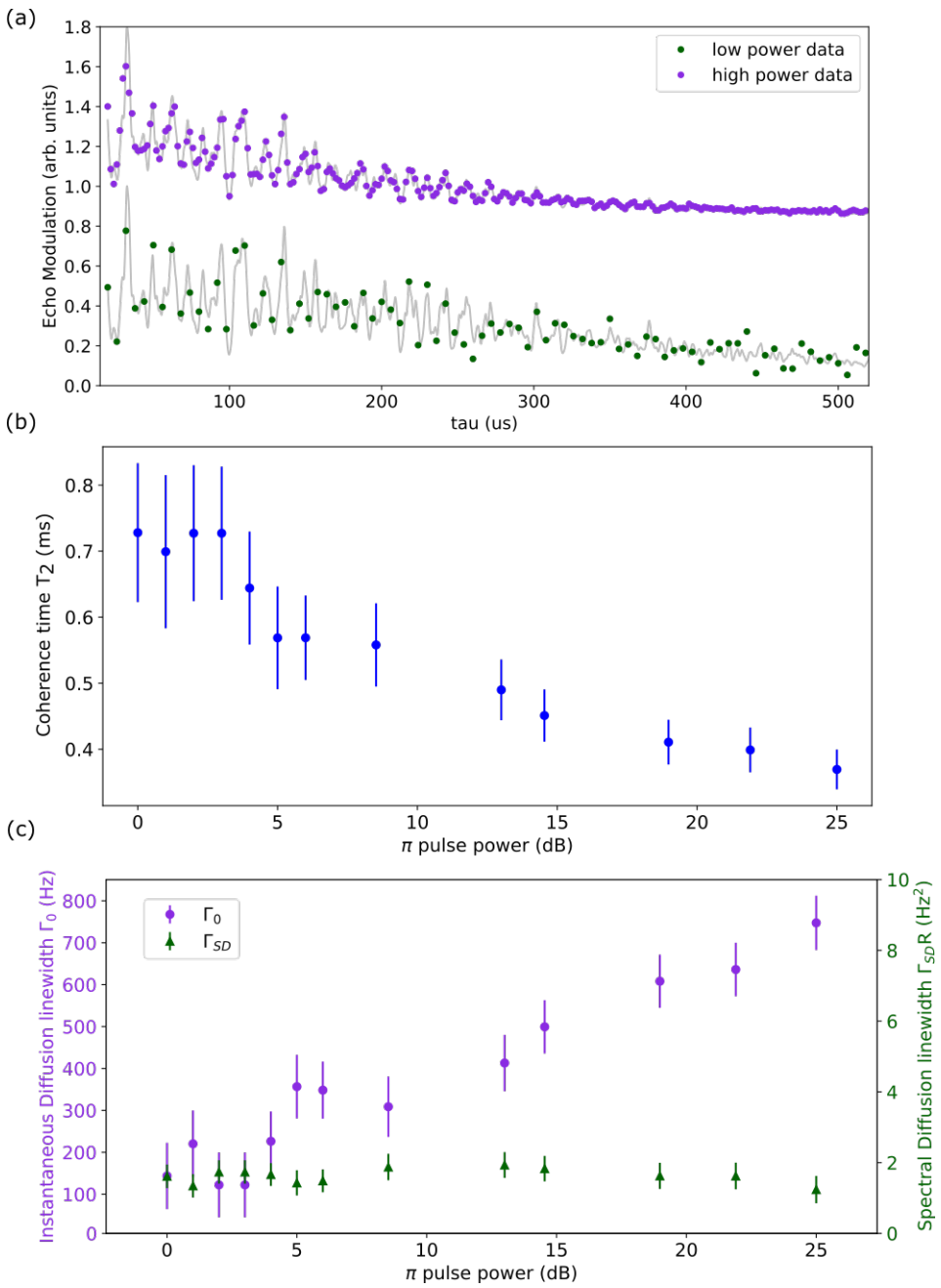

Figure 1: Two-pulse echo data recorded on the $I = 0$ ESR transition of Er^{3+} at 43mT. (a) 2PE time traces taken with high and low microwave power (0 and 25 dB). The two time traces shown here represent the average of 120 and 1000 echo measurements, for the top and bottom traces respectively. (b) 2PE coherence time as a function of applied microwave power. (c) Instantaneous and spectral diffusion contributions to the 2PE decay rate as a function of applied microwave power.

Section II: Magnetic Rotation Spectrum

Magnetic Rotation Spectroscopy (MRS) is a centuries old technique[**?**], and extremely useful for identifying particular paramagnetic species in complex and dense ESR spectra[**?**]. Here we rotate the magnetic field in the $a-c$ plane of the crystal and record ESR transmission spectra every 1.5 degrees. Several paramagnetic impurities are resolved in this way, shown by the MRS spectrum in Figure 2. Here we identify Mn^{2+} and Yb^{3+} impurities in addition to the known Er^{3+} impurities, using known Zeeman-Hamiltonian parameters, in particular g-tensors [23, 48].

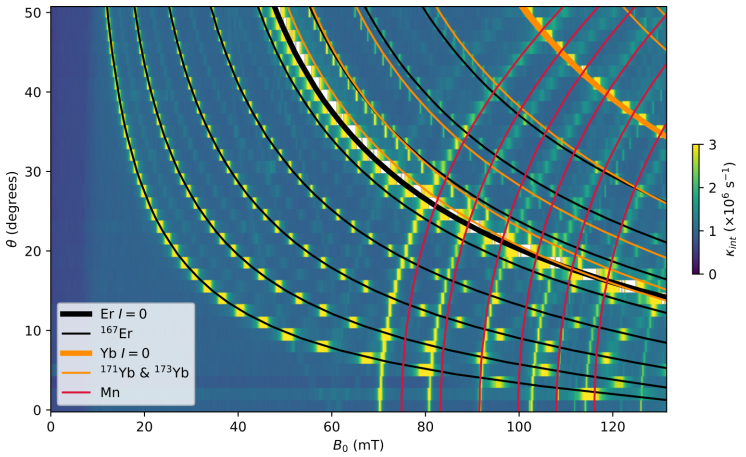

Figure 2: MRS spectrum comprising 34 continuous-wave ESR transmission spectra, each recorded as function of magnetic-field with 1.5 degree increments of field angle between each spectrum, with $\theta = 0$ corresponding to $B_0 \parallel c$. Spin transitions can be seen here by the decrease in resonator Q caused by the spin-resonator coupling. *Coloured solid lines*: Theoretical spectra of Er^{3+}, Yb^{3+} and Mn^{2+} based on spin-Hamiltonian parameters of Refs [**?**, 23, 48] respectively. For isotopes with non-zero nuclear spin (^{167}Er, ^{171}Yb and ^{173}Yb) only the nuclear-spin preserving $\Delta m_I = 0$ transitions are shown. Due to spin-state mixing, however, some weak $\Delta m_I = \pm 1$ transitions can be identified in the MRS spectrum above.

In the MSR spectrum the Mn^{2+} and Yb^{3+} impurities present six and eight ESR lines respectively. The 6 Mn^{2+} lines are attributed to the ^{55}Mn isotope, with nuclear $I = 3/2$ and 100% natural abundance. For the Yb^{3+} impurities, two lines are attributed to ^{171}Yb ($I = 1/2$, 14% nat. abun.), five lines are attributed to ^{173}Yb ($I = 5/2$, 16% nat. abun.) and the last line is a mixture of all the even isotopes between ^{168}Yb and ^{176}Yb inclusively ($I = 0$, 70% total nat. abun.). The concentrations of Yb^{3+}impurities relative to Er^{3+} can easily be determined from fits of the dominant $I = 0$ anti-crossing (refer to Section IV below). Estimates of the Mn^{2+} concentration were not attempted, however, due to its more complex electronic level structure.

Section III: Fitting the Transmission Spectra

Equation (5) of the main text can be used to independently fit both the spin-resonator coupling g_{ens} and the spin-transition linewidth Γ of several paramagnetic spin species. If the resonator parameters κ_c, $\kappa_i(B_0)$ and the spin-transition frequency $\omega_s(B_0)$ are well known, then this fit can yield very accurate results. Figure 3 presents a side-by-side example of measured and fitted transmission spectra recorded at 100mK as a function of microwave frequency $\omega_r/2\pi$ and applied magnetic field B_0. This fit is obtained by least-squares minimisation of S_{21} in the two-dimensional plane shown in Fig. 3. Here the resonator frequency ω_r is assumed to decrease quadratically with increasing magnetic field and the quadratic components are determined by a least-squares fit of S_{21} using only sections of the ESR spectrum that are devoid of spin transitions (see Fig. 2 of the main text). In this way there are only ten free parameters required to fit the spectrum shown in Figure 3 below, comprising of the (g_{ens}, Γ) pairs presented in Table 1. To obtain accurate values for these remaining ten parameters, and especially those of the smaller transitions, the fit proceeds in two steps:

1) the Er $I = 0$ is fitted alone because its large anti-crossing distorts the spectrum at the location of other nearby anti-crossings.

2) A simultaneous fitting of the other four avoided level crossings is performed with the two Er $I = 0$ parameters (g_{ens}, Γ) held fixed.

From the fit we extract the coupling parameters for the five avoided level crossings between 30-50mT, which are tabulated Table 1. Note that large differences in population between the Er $I = 0$ and the other four ensembles presented a challenge when fitting the smaller anti-crossings in the spectrum.

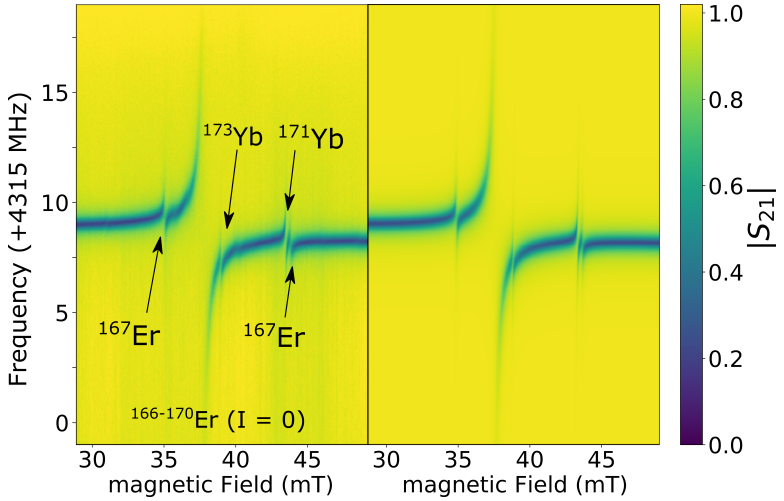

Figure 3: *Left*: A sub-section of the transmission spectrum presented in Fig. 2 of the main text, focusing on the transitions studied in Fig 3. of the main text. Five avoided level crossingss are observed in this sub-spectrum, labeled according to atomic and isotopic composition. *Right*: Fit to the transmission spectrum using Eq. (5) of the main text, assuming known Hamiltonian parameters of Er^{3+} and Yb^{3+} [**?**, 23].

Transition	g_{ens}(kHz)	Γ(MHz)
^{167}Er $\vert +1/2\rangle$	2150 ± 5	16.3 ± 0.1
$^{166-172}$Er $I = 0$	14135 ± 5	36.2 ± 0.1
^{173}Yb $\vert -5/2\rangle$	1215 ± 5	5.9 ± 0.1
^{171}Yb $\vert -1/2\rangle$	1465 ± 5	3.62 ± 0.05
^{167}Er $\vert +3/2\rangle$	2105 ± 5	22.3 ± 0.2

Table 1: Spin-resonator couplings and inhomogeneous linewidths determined at 100mK using the fit presented in Fig 3. Transitions are tabulated in order of increasing magnetic field at the avoided level crossing point. Uncertainties represent the Standard Error in the fit.

In this way g_{ens} and Γ can be measured as a function of mixing-chamber temperature, by recording the transmission spectrum at different temperatures. For the three Er transitions tabulated above, the resulting g_{ens} and Γ values in the range of 10-550mK values are presented in Fig. 3 of the main text.

Section IV: Estimating Spin Temperature and REI Impurity Concentrations

To elucidate the temperature of the electron-spin bath T_B in Fig. 3 of the main text, we compare the fitted ensemble-coupling as a function of temperature $g_{ens}(T)$ with the theoretical value of $g_{ens}(T)$ expected from Boltzmann thermal statistics. In particular, this requires a numerical determination of the spin-resonator coupling g within the volume of the calcium tungstate crystal (sub-sections 1 & 2) followed by a theoretical treatment of the temperature dependence (sub-section 3). This method further yields a direct method for determining the $\left[\mathrm{Er}^{3+}\right]$ impurity concentration, and by extension the $\left[\mathrm{Yb}^{3+}\right]$, which can be directly compared with the known impurity concentrations obtained from mass-spectrometry results presented in Table I of the main text.

Subsection IV.1: Determining the spin-resonator coupling constant 'g'

The coupling between a single spin and a harmonic oscillator follows the Jaynes-Cummings Hamiltonian [**?**]:

$$H = \hbar\omega_r \left(\hat{a}^\dagger \hat{a} + \frac{1}{2}\right) - \frac{\hbar\omega_s(B_0)}{2}\hat{\sigma}_z + \hbar g(\hat{a}\hat{\sigma}_+ + \hat{a}^\dagger\hat{\sigma}_-)$$

Here $\hat{a}^\dagger$and $\hat{a}$ represent the creation and annihilation operators of the electromagnetic field (photons) in the resonator, while $\hat{\sigma}_+$ and $\hat{\sigma}_-$ represent raising and lowering operators of the electronic spin moment $S = 1/2$. The other parameters are defined in the main text, and the coupling constant g is given as follows [**?**]:

$$g(\boldsymbol{r}) = |\langle +1/2|\delta\mathbf{B_1}(\boldsymbol{r})\cdot\boldsymbol{\gamma}\cdot\mathbf{S}|-1/2\rangle|$$

Here $\delta\mathbf{B_1}(\boldsymbol{r})$ represents the Root-Mean-Square (RMS) vacuum fluctuations of the magnetic field at the spin's position $\boldsymbol{r}$, while $\boldsymbol{\gamma}$ is the gyromagnetic-tensor. For Er^{3+}:$CaWO_4$ and Yb^{3+}:$CaWO_4$ this is given by [**?**, 23]:

$$\gamma_{\mathrm{Er}} = 2\pi \begin{pmatrix} 117 & 0 & 0 \\ 0 & 117 & 0 \\ 0 & 0 & 17.5 \end{pmatrix} \mathrm{GHz/T}$$

$$\gamma_{\mathrm{Yb}} = 2\pi \begin{pmatrix} 55.1 & 0 & 0 \\ 0 & 55.1 & 0 \\ 0 & 0 & 14.7 \end{pmatrix} \mathrm{GHz/T}$$

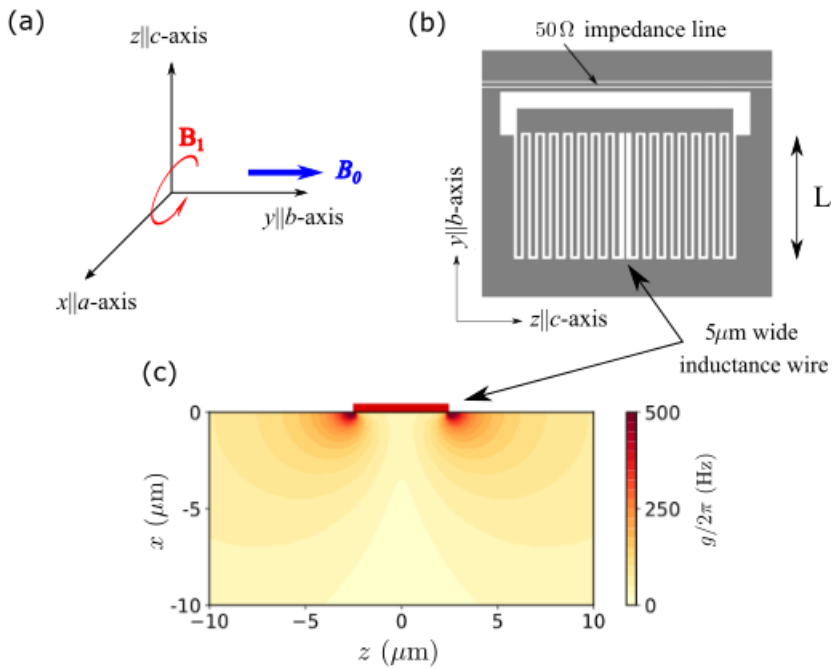

Figure 4: **(a)** Coordinate system in the (x, y, z) frame of the Spin-Hamiltonian and (a, b, c) frame of the principle crystal axes. The static magnetic field B_0 is applied along the y-axis (equivalently to the crystal b-axis) while the oscillating magnetic field B_1 only has components perpendicular to the y-axis. **(b)** Design of the superconducting resonator patterned on the surface of the $CaWO_4$ crystal, with respect to crystal axes. Dark grey shows the location of the niobium thin-film deposited on the surface, exposed crystal is shown in white**.** Microwave signals are sent and received via a 50 ohm transmission line, wirebonded on either end to SMP terminals **(c)** COMSOL simulation showing the spatial variation of the spin-resonator coupling g for the Er $I = 0$ transitions; the coupling term g is strongly correlated with the strength of the oscillating magnetic field B_1 radiating from the inductive wire. This simulation is used to calculate the 'averaged' gyromagnetic ratio $\tilde{\gamma}$**.**

The resonator generates an oscillating magnetic field $\mathbf{B_1} = \delta\mathbf{B_1}(\hat{a} + \hat{a}^\dagger)$ which is responsible for the spin-resonator interaction and whose orientation is defined by the geometry of the superconducting inductance-wire shown in 4. In the (x, y, z) basis, the vacuum fluctuations of the magnetic field are given by:

$$\delta\mathbf{B_1}(\boldsymbol{r}) = \begin{pmatrix} \delta B_{1x} \\ \delta B_{1y} \\ \delta B_{1z} \end{pmatrix}$$

for the system studied here, the static magnetic field B_0 is aligned with the y-axis and B_1 is in the (x, z)-plane, such that:

$$g(r) = \sqrt{\left(\gamma_\perp \langle S_x \rangle \delta B_{1x}\right)^2 + \left(\gamma_\parallel \langle S_z \rangle \delta B_{1z}\right)^2}$$

For the nuclear-spin-free isotopes of Er^{3+} and Yb^{3+} (i.e: the $I = 0$ transitions) the expectation values $\langle S_x \rangle$ and $\langle S_z \rangle$ can be calculated by diagonalising the Zeeman Hamiltonian $H_Z = \hbar \boldsymbol{B_0} \cdot \boldsymbol{\gamma} \cdot \boldsymbol{S}$. For the other Er electron-spin transitions, however, it's necessary to add a hyperfine interaction term to account for the coupling of the electronic-spin S to the nuclear-spin I:

$$H = \hbar \boldsymbol{B_0} \cdot \boldsymbol{\gamma} \cdot \boldsymbol{S} + \boldsymbol{S} \cdot \boldsymbol{A} \cdot \boldsymbol{I} \tag{1}$$

The hyperfine coupling matrix A can be found in ref. [**?**] and the resulting expectation values are tabulated below for the transitions studied here.

Transition	B_0 (mT)	$\langle S_x \rangle$	$\langle S_z \rangle$	$\frac{\tilde{\gamma}\hbar}{\mu_B}$
^{167}Er $\mid +1/2\rangle$	34	$-0.413i$	0.498	4.75
Er^{3+} $I = 0$	37	$-i/2$	1/2	5.71
^{167}Er $\mid +3/2\rangle$	43.5	$-0.433i$	0.498	4.98
Yb^{3+} $I = 0$	80	$-i/2$	1/2	2.75

Table 2: Expectation values $\langle S_x \rangle$ and $\langle S_z \rangle$ and 'averaged' g-factors $\tilde{g} = \frac{\tilde{\gamma}\hbar}{\mu_B}$ for the ESR transitions relevant for determining the doping concentrations of Er^{3+} and Yb^{3+}. Transitions are listed in order of increasing magnetic field B_0 in the ESR spectrum.

Subsection IV.2: Numerical estimate of the ensemble-coupling

For an ensemble of spins with homogeneous doping concentration ρ in a volume V, the ensemble-coupling g_{ens} is enhanced by a square-root factor, compared to the coupling of individual spins [31]:

$$g_{\text{ens}} = \frac{\hbar}{\mu_B}\sqrt{\rho \int_V g(r)^2 dr}$$

This expression can be expressed as a function of several experimental parameters. Firstly we can restrict the integral length along the y-axis (the b-axis of the crystal) to the length L of the inductor shown in Figure 4 (b). Moreover, we can exploit the invariance of the magnetic field B_1 along the y-axis to further simplify the integral to just two spatially varying dimensions, specifically x and z:

$$\int_V g(r)^2 dr = L \iint_{x<0} [(\gamma_\perp \langle S_x \rangle \delta B_{1x})^2 + (\gamma_\parallel \langle S_z \rangle \delta B_{1z})^2] dx dz$$

The domain can be further restricted to $x < 0$ because the spins are only located below the resonator and split the integral into two terms:

$$\iint_{x<0} [(\gamma_\perp \langle S_x \rangle \delta B_{1x})^2 + (\gamma_\parallel \langle S_z \rangle \delta B_{1z})^2] dx dz = \frac{\iint_{x<0} [(\gamma_\perp \langle S_x \rangle \delta B_{1x})^2 + (\gamma_\parallel \langle S_z \rangle \delta B_{1z})^2] dx dz}{\iint_{x<0} [\delta B_{1x}^2 + \delta B_{1z}^2] dx dz} \iint_{x<0} [\delta B_{1x}^2 + \delta B_{1z}^2] dx dz$$

Here the first term is interpreted as an 'averaged' gyromagnetic ratio, which we label $\tilde{\gamma}$:

$$\tilde{\gamma} = 2\sqrt{\frac{\iint_{x<0} [(\gamma_\perp \langle S_x \rangle \delta B_{1x})^2 + (\gamma_\parallel \langle S_z \rangle \delta B_{1z})^2] dx dz}{\iint_{x<0} [\delta B_x^2 + \delta B_z^2] dx dz}}$$

and the second term can be calculated by considering the energy of an n-photon Fock state:

$$\begin{aligned} E_n &= \hbar\omega_r (n + \frac{1}{2}) \\ &= \frac{1}{\mu_0} \int \langle n | \hat{\boldsymbol{B}}_{\mathbf{1}}(\mathbf{r})^2 | n \rangle d\mathbf{r} \\ &= \frac{1}{\mu_0} \int \langle n | \boldsymbol{\delta B}(\mathbf{r})^2 (\hat{a} + \hat{a}^\dagger)^2 | n \rangle d\mathbf{r} \\ &= \frac{2n+1}{\mu_0} \int |\boldsymbol{\delta B}(\mathbf{r})|^2 d\mathbf{r} \end{aligned}$$

which implies that:

$$\int |\boldsymbol{\delta B}(\mathbf{r})|^2 d\mathbf{r} = \frac{\mu_0 \hbar \omega_r}{2}$$

Therefore second term becomes:

$$\iint_{x<0} [\delta B_x^2 + \delta B_z^2] dx dz = \frac{1}{2L} \int |\boldsymbol{\delta B}(\mathbf{r})|^2 d\mathbf{r} = \frac{\mu_0 \hbar \omega_r}{4L}$$

and finally we arrive at a simple numeric expression for the (temperature-independent) ensemble coupling:

$$g_{\text{ens}} = \frac{\tilde{\gamma}}{4} \sqrt{\rho \mu_0 \hbar \omega_r} \tag{2}$$

This equation, which has been previously determined in Ref [31], links the ensemble coupling constant to the erbium concentration ρ. The 'averaged' spin-resonator coupling term$\tilde{g}$ is computed using a COMSOL simulation of the magnetic field B_1 over a $400 \times 200\,\mu m^2$ area representing $x \times z$ and assuming a 5 μm wide wire. This simulation includes the expectation values of the spin-matrix elements presented in the third and fourth columns of Table 2 and an example of such a simulation is presented in Figure 4 (c) for the Er $I = 0$ transition. The calculated values of $\tilde{\gamma}$ are presented in the fifth column of Table 2.

Subsection IV.3: Fitting the temperature dependence of g_{ens}

Equation 2 assumes complete polarisation of the electron-spins within the ensemble. In reality the spin-polarisation P is temperature dependent, and Eq. 2 should be adjusted to reflect this:

$$g_{\text{ens}}(T) = \frac{\tilde{\gamma}}{4} \sqrt{P(T) \rho \mu_0 \hbar \omega_0} \tag{3}$$

Assuming a Boltzmann thermal distribution, the thermal polarisation of the nuclear-spin-free Er and Yb isotopes (i.e: the $I = 0$ transitions) is described by a hyperbolic tangent function:

$$\begin{aligned} P(T, I = 0) &= \tanh\left(\frac{\hbar \gamma B_0}{2kT_B}\right) \\ &= \tanh\left(\frac{\hbar \omega_r}{2kT_B}\right) \end{aligned}$$

where the usual thermal limits apply:

$$\begin{aligned} \lim_{T \to 0} P(T, I = 0) &= 1 \\ \lim_{T \to \infty} P(T, I = 0) &= 0 \end{aligned}$$

For the electron-spin transitions between hyperfine levels of ^{167}Er, however, one must consider all 16 hyperfine states defined by their spin-projection $|m_S, m_I\rangle$. This is necessary because the small applied magnetic field used in these experiments can allow all $(2S+1)(2I+1) = 16$ hyperfine levels to be populated at high temperatures. For a given electron-spin transition of a nuclear-spin projection $|m_I\rangle$ the thermal polarisation then follows the general Boltzmann form:

$$P(T, m_I) = \frac{\exp[-E_{|+1/2, mI\rangle}/(kT)] - \exp[-E_{|-1/2, mI\rangle}/(kT)]}{\sum_{(2S+1)(2I+1)} \exp[-E_{|mS, mI\rangle}/(kT)]} \tag{4}$$

where the energies $E_{|m_S, m_I\rangle}$ is the energy of hyperfine level $|m_S, m_I\rangle$ at the magnetic field B_0 for which g_{ens} is measured. The fit to the g_{ens} data presented in Fig. 3 of the main text relies on additional knowledge of the relative concentration of the^{167}Er and $I = 0$ Er isotopes, ρ_{Er-167} and $\rho_{Er,I=0}$ respectively. In this way all three transitions are fitted simultaneously with a single free parameter $\rho = \rho_{Er-167} + \rho_{Er,I=0}$ where:

$$\begin{aligned} \rho &= \rho_{Er-167} + \rho_{Er,I=0} \\ &= 4.37 \rho_{Er-167} \\ &= 1.3 \rho_{Er,I=0} \end{aligned}$$

This yields an erbium concentration $\left[\mathrm{Er}^{3+}\right] = 2.26 \times 10^{17}\,\mathrm{cm}^{-3}$ or equivalently 18 ppm relative doping. This is very similar to the Er doping concentration determined by mass-spectrometry, presented in Table I of the main text.

Sub-section 4: Determining the Yb^{3+} concentration

With an estimated erbium concentration of 18 ppm, it is possible to further estimate the concentration of ytterbium by considering the relative values of $\tilde{\gamma}$ and g_{ens} of the nuclear-spin-free ($I = 0$) ESR transitions for the two spin species:

$$\frac{g_{ens}(\mathrm{Er})}{g_{ens}(\mathrm{Yb})} = \frac{\tilde{\gamma}(\mathrm{Er})}{\tilde{\gamma}(\mathrm{Yb})} \frac{\sqrt{0.77\left[\mathrm{Er}^{3+}\right]}}{\sqrt{0.7\left[\mathrm{Yb}^{3+}\right]}}$$

$$\Rightarrow \left[\mathrm{Yb}^{3+}\right] = 1.1\left[\mathrm{Er}^{3+}\right]\left(\frac{g_{ens}(\mathrm{Yb})\tilde{\gamma}(\mathrm{Er})}{g_{ens}(\mathrm{Er})\tilde{\gamma}(\mathrm{Yb})}\right)^2$$

substituting the known values gives

$$\left[\mathrm{Yb}^{3+}\right] = 1.29 \times 10^{17}\,\mathrm{cm}^{-3}$$

or equivalently, 10 ppm relative doping of Yb^{3+}.

Section V : Fitting the Three Pulse Echo data

An accurate analysis of spectral diffusion in the millikelvin temperature range requires that at least the Er and Yb $I = 0$ sub-species be taken into account in Eq. (2) of the main text. Both are required because they exist in similar ppm concentrations (22.9 and 14.1 ppm, respectively) while demonstrating very different gyromagnetic ratios and therefore neither population is expected to dominate the spectral diffusion processes across the entire millikelvin temperature range. This assumption yields four spectral diffusion parameters : $\Gamma_{\mathrm{SD}}^{Er}$, R^{Er}, $\Gamma_{\mathrm{SD}}^{Yb}$ & R^{Yb}, however, the physical similarity between these rare earth impurities implies that the number of free parameters required to fit Eq. (2) is no greater than for a single spin-species; namely two. In particular, this fitting proceeds at each measured spin-bath temperature T_B by assuming a relationship between the spectral diffusion linewidths Γ_{SD} governed by Eq. (3) of the main text:

$$\frac{\Gamma_{\mathrm{SD}}^{Yb}}{\Gamma_{\mathrm{SD}}^{Er}} = \frac{\Gamma_{\mathrm{max}}^{Yb}\mathrm{sech}^2\left(g_{\mathrm{Yb}}\mu_B B_0\left(2kT_B\right)^{-1}\right)}{\Gamma_{\mathrm{max}}^{Er}\mathrm{sech}^2\left(g_{\mathrm{Er}}\mu_B B_0\left(2kT_B\right)^{-1}\right)}$$

Where $\Gamma_{\mathrm{max}}^{S}$ represents the maximum spectral-diffusion linewidth, for which we assume an analytic form derived by Maryasov et. al. [**?**]:

$$\Gamma_{\mathrm{max}}^{S} = \frac{\mu_B^2 \mu_0 g_{\mathrm{Er}} g_{\mathrm{S}} n_{\mathrm{S}}}{9\sqrt{3}\hbar} \tag{5}$$

Noting that the first g-factor is fixed for both species and determined by the densest and most perturbative paramagnetic species in the matrix (the erbium species), the spectral-diffusion contribution of the ytterbium spins can be re-parametrised at each temperature T_B as a function of the erbium contribution $\Gamma_{\mathrm{SD}}^{Er}$ and known impurity concentrations n_{S}:

$$\Gamma_{\mathrm{SD}}^{Yb} = \Gamma_{\mathrm{SD}}^{Er}\frac{g_{\mathrm{Yb}} n_{\mathrm{Yb}}\mathrm{sech}^2\left(g_{\mathrm{Yb}}\mu_B B_0\left(2kT_B\right)^{-1}\right)}{g_{\mathrm{Er}} n_{\mathrm{Er}}\mathrm{sech}^2\left(g_{\mathrm{Er}}\mu_B B_0\left(2kT_B\right)^{-1}\right)} \tag{6}$$

A similar treatment using Eq. (4) of the main text (and neglecting the spin-lattice contribution) gives the following relationship for the spin-flip rate R :

$$R^{Yb} = R^{Er}\frac{\Gamma_{\rm Er}}{\Gamma_{\rm Yb}}\frac{g_{\rm Yb}^4 n_{\rm Yb}^2 \mathrm{sech}^2\left(g_{\rm Yb}\mu_B B_0 \left(2kT_B\right)^{-1}\right)}{g_{\rm Er}^4 n_{\rm Er}^2 \mathrm{sech}^2\left(g_{\rm Er}\mu_B B_0 \left(2kT_B\right)^{-1}\right)} \tag{7}$$

where $\Gamma_{\rm Er} = 36.5$MHz & $\Gamma_{\rm Yb} = 5.6$MHz represent the inhomogeneous Er $I = 0$ and Yb $I = 0$ transition linewidths respectively, measured at 100mK[1].

Using the relationships defined above it was possible to obtain unique solutions to $\Gamma_{\rm SD}^{Er}$ and R^{Er}(and by extension $\Gamma_{\rm SD}^{Yb}$ & R^{Yb}) using Eq. (2) and fitting to families of four (or more) three-pulse-echo decay curves at a fixed temperature. Examples of this fitting for three different temperatures are presented in Figure 4 of the main text.

Section VI : Decoherence rate model

The model of decoherence rate (i.e homogeneous linewidth) Γ_h presented in Fig. 5c of the main text is comprised of three contributions. In particular, these are the instantaneous-diffusion decoherence rate Γ_0, the electron-spin spectral diffusion decoherence rate $\Gamma(SD)$ and the nuclear-spin spectral diffusion decoherence rate $\Gamma(NSD)$. To combine these contributions we utilise the T_2 formulation presented in Eq. 6 of the main text, together with the decoherence-rate formalism $\Gamma_h = 1/\pi T_2$,

$$\Gamma_h = \frac{2\Gamma(SD)^2 + 2\Gamma(NSD)^2}{-\Gamma_0 + \sqrt{\Gamma_0^2 + 4\Gamma(SD)^2 + 4\Gamma(NSD)^2}}.$$

The contribution Γ_0 is based on the analytic expression presented in Chapter 3 of the PhD Thesis of M. Le Dantec [**?**], following the approach used by Tyryshkin *et. al.* [45]:

$$\Gamma_0 = \frac{9\sqrt{3}\hbar}{\mu_0\left(g_{eff}\mu_B\right)^2}\frac{\Gamma_{|+3/2\rangle}}{\Delta\omega}c_{|+3/2\rangle}\sin^{-2}\left(\frac{\theta_2}{2}\right)$$

Here $g_{eff} \approx g_\perp = 8.38$ is the effective g-factor in the direction of the applied field magnetic field. The ratio $\Gamma_{|+3/2\rangle}/\Delta\omega$ represents the ratio of the inhomogeneous ESR transition linewidth $\Gamma_{|+3/2\rangle} \approx 22$ MHz to pulse-exitation bandwidth $\Delta\omega = 700$ kHz. Furthermore, the spin-density $c_{|+3/2\rangle} = P(T, |+3/2\rangle)\rho_{167}$ represents the temperature-dependent density of the $m_I = |+3/2\rangle$ hyperfine sub-level. It comprises the product of the spin-polarisation $P(T, |+3/2\rangle)$ given in Eq. 4 and the ^{167}Er defect density $\rho_{167} = 5.2\cdot10^{16}\,\mathrm{cm}^{-3}$, determined from Table I of the main text. Finally, the angle $\theta_2 = 1.9$ rads is the average rabi-angle of the π pulse used during echo measurements: a value determined numerically for the inhomogeneous B_1 field generated by the microwave resonator [**?**]. Generally speaking, the decoherence contribution Γ_0 increases with temperature and plateaus to a value of 650 Hz at approximately 700mK, once all 16 hyperfine states of ^{167}Er are equally populated.

For the electron-spin contribution $\Gamma(SD)$ we consider only the Er $I = 0$ and Yb $I = 0$ spin baths, and infer a temperature-dependent rate:

$$\Gamma(SD) = \sqrt{\frac{1}{4\pi}\left(\Gamma_{\rm SD}^{Er}R^{Er} + \Gamma_{\rm SD}^{Yb}R^{Yb}\right)}$$

for this contribution we further assume that the spectral-diffusion linewidth $\Gamma_{\rm SD}^S$ and rate R^S has a temperature dependence following Eq. (3) and Eq. (4) of the main text:

$$\Gamma_{\rm SD}^S R^S(T_B) = \Gamma_{max}^S R_{max}^S \mathrm{sech}^4\left(\frac{\hbar\gamma_S B_0}{2kT_B}\right)$$

[1] See Figure 3 of the main text for examples the inhomogeneous erbium linewidth measured at various temperatures.

Here we determine the values of Γ^S_{max} and R^S_{max} using solely the analysis of the 3PE measurements. In particular, we take the values presented by the dashed-line fits of Fig. 5a and b of the main text. This yields $\Gamma^{Er}_{max} = 400$ kHz, $R^{Er}_{max} = 1.4\,\mathrm{ms}^{-1}$ and $\Gamma^{Yb}_{max} = 150$ kHz, $R^{Yb}_{max} = 0.14\,\mathrm{ms}^{-1}$ for Er for Yb contributions, respectively.

Finally, we estimate the nuclear-spin contribution from the cluster-correlated-expansion (CCE) simulation of the ^{183}W nuclear-spin bath presented in Fig. 2a of Ref. [19]:

$$\begin{aligned}\Gamma(NSD) &= \frac{1}{\pi \cdot 27 \cdot 10^{-3}\,s} \\ &= 12\,\mathrm{Hz}\end{aligned}$$

Although this CCE simulation was undertaken for the Er $I = 0$ transition, rather than the $m_I = |+3/2\rangle$ transition, it is still a valid estimate given the similarity of the transition-dipole moments presented in Table 2 above. Note also that this contribution is temperature independent because the ^{183}W nuclear-spin bath remains unpolarised at millikelvin temperatures.

References

[1] Zhong, M. *et al.* Optically addressable nuclear spins in a solid with a six-hour coherence time. *Nature* **517**, 177–180 (2015). URL `http://dx.doi.org/10.1038/nature14025`.

[2] Holzäpfel, A. *et al.* Optical storage for 0.53 s in a solid-state atomic frequency comb memory using dynamical decoupling. *New Journal of Physics* **22**, 063009 (2020). URL `https://iopscience.iop.org/article/10.1088/1367-2630/ab8aachttps://iopscience.iop.org/article/10.1088/1367-2630/ab8aac/meta`. `1910.08009`.

[3] Longdell, J. J., Fraval, E., Sellars, M. J. & Manson, N. B. Stopped Light with Storage Times Greater than One Second Using Electromagnetically Induced Transparency in a Solid. *Physical Review Letters* **95**, 063601 (2005). URL `http://link.aps.org/doi/10.1103/PhysRevLett.95.063601`.

[4] Rančić, M., Hedges, M. P., Ahlefeldt, R. L. & Sellars, M. J. Coherence time of over a second in a telecom-compatible quantum memory storage material. *Nature Physics* **14**, 50–54 (2018). URL `http://www.nature.com/doifinder/10.1038/nphys4254`.

[5] Hedges, M. P., Longdell, J. J., Li, Y. & Sellars, M. J. Efficient quantum memory for light. *Nature* **465**, 1052–1056 (2010). URL `http://www.ncbi.nlm.nih.gov/pubmed/20577210http://dx.doi.org/10.1038/nature09081`.

[6] Dajczgewand, J., Le Gouët, J.-L., Louchet-Chauvet, A. & Chanelière, T. Large efficiency at telecom wavelength for optical quantum memories. *Optics Letters* **39**, 2711 (2014). URL `https://www.osapublishing.org/abstract.cfm?URI=ol-39-9-2711`.

[7] Sabooni, M., Li, Q., Kröll, S. & Rippe, L. Efficient Quantum Memory Using a Weakly Absorbing Sample. *Physical Review Letters* **110**, 133604 (2013). URL `http://link.aps.org/doi/10.1103/PhysRevLett.110.133604`.

[8] Bartholomew, J. G. *et al.* On-chip coherent microwave-to-optical transduction mediated by ytterbium in YVO4. *Nature Communications* **11**, 1–6 (2020). URL `https://www.nature.com/articles/s41467-020-16996-x`. `1912.03671`.

[9] Fernandez-Gonzalvo, X., Horvath, S. P., Chen, Y. H. & Longdell, J. J. Cavity-enhanced Raman heterodyne spectroscopy in Er^{3+}:Y_2SiO_5 for microwave to optical signal conversion. *Physical Review A* **100**, 033807 (2019). `1712.07735`.

[10] Grezes, C. *et al.* Towards a spin-ensemble quantum memory for superconducting qubits (2016). `1510.06565`.

[11] Sigillito, A. J. *et al.* Fast, low-power manipulation of spin ensembles in superconducting microresonators. *Applied Physics Letters* **104**, 222407 (2014). URL http://aip.scitation.org/doi/10.1063/1.4881613. 1403.0018.

[12] Grèzes, C. *Towards a spin ensemble quantum memory for superconducting qubits.* Phd thesis, Universite Paris-Saclay (2015).

[13] Ranjan, V. *et al.* Electron spin resonance spectroscopy with femtoliter detection volume. *Applied Physics Letters* **116**, 184002 (2020). URL https://aip.scitation.org/doi/abs/10.1063/5.0004322.

[14] Probst, S., Rotzinger, H., Ustinov, A. V. & Bushev, P. A. Microwave multimode memory with an erbium spin ensemble. *Physical Review B - Condensed Matter and Materials Physics* **92**, 014421 (2015). URL https://journals.aps.org/prb/abstract/10.1103/PhysRevB.92.014421. 1501.01499.

[15] Dold, G. *milliKelvin ESR of rare-earth doped crystals using superconducting resonators.* Phd thesis, University College London (2020).

[16] Li, P. Y. *et al.* Hyperfine Structure and Coherent Dynamics of Rare-Earth Spins Explored with Electron-Nuclear Double Resonance at Subkelvin Temperatures. *Physical Review Applied* **13**, 024080 (2020). 1910.12351.

[17] Rakonjac, J. V., Chen, Y.-H., Horvath, S. P. & Longdell, J. J. Long spin coherence times in the ground state and in an optically excited state of $^{167}Er^{3+}$:Y_2SiO_5 at zero magnetic fields. *Physical Review B* 184430 (2020). URL https://journals.aps.org/prb/abstract/10.1103/PhysRevB.101.184430.

[18] Ortu, A. *et al.* Simultaneous coherence enhancement of optical and microwave transitions in solid-state electronic spins. *Nature Materials 2018 17:8* **17**, 671–675 (2018). URL https://www.nature.com/articles/s41563-018-0138-x. 1712.08615.

[19] Dantec, M. L. *et al.* Twenty-three millisecond electron spin coherence of erbium ions in a natural-abundance crystal. *Science Advances* **7**, 9786 (2021). URL https://www.science.org/doi/full/10.1126/sciadv.abj9786. 2106.14974.

[20] Kanai, S. *et al.* Generalized scaling of spin qubit coherence in over 12,000 host materials (2021). URL https://arxiv.org/abs/2102.02986v1. 2102.02986.

[21] Herzog, B. & Hahn, E. L. Transient nuclear induction and double nuclear resonance in solids. *Physical Review* **103**, 148–166 (1956).

[22] Ferrenti, A. M., de Leon, N. P., Thompson, J. D. & Cava, R. J. Identifying candidate hosts for quantum defects via data mining. *npj Computational Materials* **6**, 1–6 (2020). URL https://www.nature.com/articles/s41524-020-00391-7. 2006.14128.

[23] Kiel, A. & Mims, W. B. Electric-Field-Induced g Shifts for Loose Yb Ions in Three Scheelite Lattices. *Physical Review B* **1**, 2935–2944 (1970). URL https://link.aps.org/doi/10.1103/PhysRevB.1.2935.

[24] Bertaina, S. *et al.* Rare-earth solid-state qubits. *Nature Nanotechnology* **2**, 39–42 (2007). URL http://www.nature.com/doifinder/10.1038/nnano.2006.174http://www.nature.com/articles/nnano.2006.174.

[25] Guillot-Noël, O. *et al.* Hyperfine interaction of Er^{3+} ions in Y_2:SiO_5 : An electron paramagnetic resonance spectroscopy study. *Physical Review B* **74**, 214409 (2006). URL http://link.aps.org/doi/10.1103/PhysRevB.74.214409.

[26] Macklin, C. *et al.* A near-quantum-limited Josephson traveling-wave parametric amplifier. *Science* **350**, 307–310 (2015).

[27] Probst, S. *et al.* Inductive-detection electron-spin resonance spectroscopy with $65 spins/\sqrt{Hz}$ sensitivity. *Applied Physics Letters* **111**, 202604 (2017). URL http://aip.scitation.org/doi/10.1063/1.5002540. 1708.09287.

[28] Bienfait, A. *et al.* Reaching the quantum limit of sensitivity in electron spin resonance. *Nature nanotechnology* **11**, 253–257 (2015). URL http://www.nature.com/doifinder/10.1038/nnano.2015.282. 1507.06831.

[29] Song, C. *et al.* Microwave response of vortices in superconducting thin films of Re and Al. *Physical Review B - Condensed Matter and Materials Physics* **79**, 174512 (2009). URL https://journals.aps.org/prb/abstract/10.1103/PhysRevB.79.174512. 0812.3645.

[30] Probst, S. *et al.* Anisotropic rare-earth spin ensemble strongly coupled to a superconducting resonator. *Physical review letters* **110**, 157001 (2013). URL https://link.aps.org/doi/10.1103/PhysRevLett.110.157001https://journals.aps.org/prl/abstract/10.1103/PhysRevLett.110.157001.

[31] Kubo, Y. *et al.* Strong Coupling of a Spin Ensemble to a Superconducting Resonator. *Physical Review Letters* **105**, 140502 (2010). URL https://link.aps.org/doi/10.1103/PhysRevLett.105.140502.

[32] Mims, W. B., Nassau, K. & McGee, J. D. Spectral Diffusion in Electron Resonance Lines. *Physical Review* **123**, 2059 (1961). URL https://journals.aps.org/pr/abstract/10.1103/PhysRev.123.2059.

[33] Hu, P. & Hartmann, S. R. Theory of spectral diffusion decay using an uncorrelated-sudden-jump model. *Physical Review B* **9**, 1 (1974). URL https://journals.aps.org/prb/abstract/10.1103/PhysRevB.9.1.

[34] Böttger, T., Thiel, C. W., Sun, Y. & Cone, R. L. Optical decoherence and spectral diffusion at 1.5 μm in Er^{3+}:Y_2SiO_5 versus magnetic field, temperature, and Er^{3+} concentration. *Physical Review B* **73**, 075101 (2006). URL http://link.aps.org/doi/10.1103/PhysRevB.73.075101.

[35] Bai, Y. S. & Fayer, M. D. Time scales and optical dephasing measurements: Investigation of dynamics in complex systems. *Physical Review B* **39**, 11066 (1989). URL https://journals.aps.org/prb/abstract/10.1103/PhysRevB.39.11066.

[36] Probst, S. *et al.* Hyperfine spectroscopy in a quantum-limited spectrometer. *Magnetic Resonance* **1**, 315–330 (2020). 2001.04854.

[37] Angeletti, B. & Ambrosi, J. P. European Centre for Environmental Geoscience Research and Teaching (2020). URL https://www.cerege.fr/en/analytic-facilities/la-icp-ms-platform-elemental-chemistry.

[38] Dantec, M. L. *Electron spin dynamics of erbium ions in scheelite crystals , probed with superconducting resonators at millikelvin temperatures.* Ph.D. thesis, Université Paris-Saclay (2022). URL https://tel.archives-ouvertes.fr/tel-03579857.

[39] Car, B., Veissier, L., Louchet-Chauvet, A., Le Gouët, J. L. & Chanelière, T. Optical study of the anisotropic erbium spin flip-flop dynamics. *Physical Review B* **100**, 165107 (2019). URL https://journals.aps.org/prb/abstract/10.1103/PhysRevB.100.165107. 1811.10285.

[40] Mims, W. B. & Gillen, R. Broadening of paramagnetic-resonance lines by internal electric fields. *Physical Review* **148**, 438–443 (1966). URL https://journals.aps.org/pr/abstract/10.1103/PhysRev.148.438.

[41] Baibekov, E. I. *et al.* Broadening of paramagnetic resonance lines by charged point defects in neodymium-doped scheelites. *Optics and Spectroscopy* **116**, 661–666 (2014). URL http://link.springer.com/10.1134/S0030400X1405004X.

[42] Ranjan, V. *et al.* Probing Dynamics of an Electron-Spin Ensemble via a Superconducting Resonator. *Physical Review Letters* **110**, 067004 (2013). URL https://link.aps.org/doi/10.1103/PhysRevLett.110.067004. 1208.5473.

[43] Zech, M., Schoebel, J. & Pickert, T. Stick-slip drive, especially pieze-actuated inertial drive (2019). URL https://patents.google.com/patent/US10505470B2/en.

[44] Kurshev, V. V. & Ichikawa, T. Effect of spin flip-flop on electron-spin-echo decay due to instantaneous diffusion. *Journal of Magnetic Resonance (1969)* **96**, 563–573 (1992).

[45] Tyryshkin, A. M. *et al.* Electron spin coherence exceeding seconds in high-purity silicon. *Nature Materials 2011 11:2* **11**, 143–147 (2011). URL `https://www.nature.com/articles/nmat3182`.

[46] Yang, W. & Liu, R. B. Quantum many-body theory of qubit decoherence in a finite-size spin bath. *Physical Review B - Condensed Matter and Materials Physics* **78**, 085315 (2008). `0806.0098`.

[47] Yang, W. & Liu, R. B. Quantum many-body theory of qubit decoherence in a finite-size spin bath. II. Ensemble dynamics. *Physical Review B - Condensed Matter and Materials Physics* **79**, 115320 (2009). `0902.3055`.

[48] Hempstead, C. F. & Bowers, K. D. Paramagnetic resonance of impurities in CaWO4. I. Two S-state ions. *Physical Review* **118**, 131–134 (1960).